Verification of the Non-local Avalanche Current Model in Mextram for Advanced SiGe HBTs

Dhariyash Rathod

Master of Science Thesis

TU Delft
Delft University of Technology

EEMCS

Verification of the Non-local Avalanche Current Model in Mextram for Advanced SiGe HBTs

Master of Science Thesis

For the degree of Master of Science in Electrical Engineering
at Delft University of Technology

Dhariyash Rathod

December 18, 2013

Faculty of Electrical Engineering, Mathematics and Computer Science
Delft University of Technology

Copyright © Microelectronics
All rights reserved.

Delft University of Technology
Department of Microelectronics

The undersigned hereby certify that they have read and recommend to the Faculty of Electrical Engineering, Mathematics and Computer Science for acceptance a thesis entitled

Verification of the Non-local Avalanche Current Model in Mextram for Advanced SiGe HBTs

by

Dhariyash Rathod

in partial fulfillment of the requirements for the degree of

Master of Science

Dated: December 18, 2013

Supervisor(s):

dr. ir. R. van der Toorn (Assistant Professor, TU Delft)

PDEng. ir. R. Setekera (PhD Candidate, TU Delft)

Reader(s):

prof. dr. R. Dekker (Professor, TU Delft)

dr. J. Hoekstra (Associate Professor, TU Delft)

prof. dr. J.W. Slotboom (Professor Emeritus, TU Delft)

To ‘Pappa’, for being my real life hero.
And ‘Mummy’, for all her love and sacrifices .

“The only way to discover the limits of the possible is to go beyond them into the impossible."

— *Sir Arthur Charles Clarke*

Abstract

To realize optimum performance, SiGe HBTs are typically designed with heavily doped implanted collectors. For practical circuits operating at either high collector current density (J_c) or high collector-base voltage (V_{cb}) avalanche multiplication is an important effect that must be accurately measured and modeled. For example in digital applications, the avalanche multiplication factor (M-1) determines the breakdown voltage, which in turn determines the maximum power supply for stable logic operation. In critical RF circuits such as power amplifiers (PA) and low noise amplifiers (LNA), the base-collector junction avalanche multiplication degrades the linearity of the circuit because of the resulting strong non-linear feedback from the output (collector) to input (base). This is particulary the case for state-of-art high-performance transistors featuring high collector doping. Therefore the accuracy of avalanche multiplication models in different operational conditions is critical to devices design of high linearity LNA and PA circuits.

In this thesis, the temperature dependence of the avalanche current in Mextram compact model is addressed. Through extensive DC measurements over temperature on advanced industrial SiGe HBTs, it was discovered that the current local-electric field based avalanche current model in the Mextram model is incapable of describing the avalanche current as a function of device temperature. This setback is the key motivation behind the work in this thesis.

By employing the simplified energy-balance equation, the impact ionization rate (α) was expressed in terms of the carrier (electron for NPN HBT) energy or temperature (T_e). Here a triangular shaped electric field distribution corresponding to the normal forward operation regime was assumed. Taking the integral of the electron temperature dependent ionization rate over the epilayer yielded the non-local multiplication factor. The product of the multiplication factor with epilayer current gives the non-local avalanche current, which takes non-local avalanche effects into account. The compact formulation of this non-local avalanche current model was derived and implemented at Delft University of Technology in the in-house version of Mextram compact model.

An extended experimental verification of the new compact model for the non-local avalanche current implemented in Mextram was carried out for different advanced SiGe HBT technologies; and the results are presented in this thesis. Verification results showed that the non-local avalanche current model can accurately describe the avalanche current as a function of temperature for different SiGe HBTs (both NPN and PNP). These results implies that the observed setback in Mextram model with respect to the temperature dependence of the avalanche current can be fully addressed by taking non-local avalanche effects into account.

Contents

Contents **iii**

List of Figures **v**

List of Tables **ix**

1 Introduction **1**
- 1.1 Trade-off Between Transistor Speed and Breakdown 1
- 1.2 Avalanche Breakdown in Bipolar Junction Transistors 3
- 1.3 Compact Modeling in Bipolar Junction Transistors 3
- 1.4 Research Goals and Objectives 5
- 1.5 Thesis Organization 6

2 DC Measurements and Mextram Simulation Results **7**
- 2.1 DC Measurement Set-up 7
- 2.2 Parameter Extraction in Mextram Compact Model 9
- 2.3 Analysis of the Temperature Dependence of Avalanche Current in Mextram Model 12
  - 2.3.1 Measured and Simulated Base Current for HVCOM (NPN) SiGe HBT 13
  - 2.3.2 Measured and Simulated Base Current for HS (NPN) SiGe HBT . . . 14
  - 2.3.3 Measured and Simulated Base Current for RFCOM (NPN) SiGe HBT 15
  - 2.3.4 Measured and Simulated Base Current for HVCOM (PNP) SiGe HBT 16
- 2.4 Discussion 16
- 2.5 Conclusion 17

3 Modeling Local and Non-local Avalanche Current in Bipolar Junction Transistors **19**

3.1 Avalanche Process in Bipolar Junction Transistors 19
3.2 Modeling (Local) Avalanche Current in Mextram Model 21
3.3 Modeling Non-local Base-Collector Avalanche Current 26
3.3.1 Determination of Electron Temperature $T_e(x)$ 27
3.3.2 Multiplication Factor 29
3.3.3 Compact Model for the Non-local Avalanche Current 30
3.4 Temperature Scaling of the Relaxation Length (λ_e) in Mextram Model 30
3.5 Summary 31

4 Verification of the Non-local Avalanche Model in Mextram 33
4.1 Parameter Extraction for the Non-local Avalanche Model in Mextram 33
4.2 Theoretical Calculation of the Built-in Voltage (V_{bi}) 35
4.3 Numerical Error Analysis for HS SiGe HBT 36
4.4 Verification of Non-Local Avalanche Current Model 37
4.4.1 Verification for HVCOM (NPN) SiGe HBT 37
4.4.2 Verification Results for HS (NPN) SiGe HBT 39
4.4.3 Verification Results for RF (NPN) SiGe HBT 41
4.4.4 Verification Results for HVCOM (PNP) SiGe HBT 43
4.5 Discussion 45
4.6 Conclusion 46

5 Conclusion and Recommendations 47
5.1 Conclusions 47
5.2 Main Findings 48
5.3 Recommendations 48

A Measurement and Simulation Results for HVCOM SiGe HBTs 51
A.1 Measurement and Simulation Result for HVCOM (NPN) SiGe HBT 51
A.1.1 Depletion Capacitance Measurements and Mextram Simulations Results 51
A.1.2 Forward Gummel Measurement and Mextram Simulation 53
A.1.3 Reverse Gummel Measurement and Mextram Simulation 54
A.1.4 Forward Early Measurement and Mextram Simulation 56
A.1.5 Output Characteristics Measurements and Mextram Simulations . . 56
A.2 Measurement and Simulation Result for HVCOM (PNP) SiGe HBT 58
A.2.1 Depletion Capacitance Measurement and Mextram Simulation Results 58
A.2.2 Forward Gummel Measurement and Mextram Simulation Results . 60
A.2.3 Reverse Gummel Measurement and Mextram Simulation Results . . 61
A.2.4 Forward Early Measurement and Mextram Simulations Results . . . 63
A.2.5 Output Characteristics Measurement and Mextram Simulation Results 63

Bibliography 65

Acknowledgments

List of Figures

1-1 The cut-off frequency as a function of collector-to-emitter breakdown voltage with open base for integrated self-aligned SiGe HBT and SiGeC HBT technologies [1]. 2

2-1 Measured (symbols) and simulated (solid lines) base current as a function of collector-base voltage (V_{cb}) and device temperature for HVCOM (NPN) SiGe HBT. Here, $V_{BE} = 0.65V$ and $T \in \{-25, 0, 25, 50, 75, 100, 125\}$ °C. Due to the perfect fit, the simulation results overlaps with the measurement results so they are not visible. 13
2-2 Measured (symbols) and simulated (solid lines) base current as a function of collector-base voltage (V_{cb}) and device temperature for HS (NPN) SiGe HBT. Here, $V_{BE} = 0.65V$ and $T \in \{25, 50, 75, 100, 125\}$ °C. 14
2-3 Measured (symbols) and simulated (solid lines) base current as a function of collector-base voltage (V_{cb}) and device temperature for RFCOM (NPN) SiGe HBT. Here, $V_{BE} = 0.65V$ and $T \in \{25, 50, 75, 100, 125\}$ °C. 15
2-4 Measured (symbols) and simulated (solid lines) base current as a function of collector-base voltage (V_{cb}) and device temperature for HVCOM (PNP) SiGe HBT. Here, $V_{BE} = 0.65V$ and $T \in \{25, 50, 75, 100, 125\}$ °C. 16

3-1 Schematic representation of the avalanche multiplication process in an NPN bipolar transistor 20
3-2 The full Mextram equivalent circuit for the vertical NPN transistor. The local avalanche current is represented by a current source I_{avl} (dashed circle). . . . 21
3-3 Schematic representation of the absolute value of the electric field used in the derivation of local Mextram avalanche model [2]. 24
3-4 Normalized electron temperature, local-electric field, and non-local impact ionization rate in the epi-collector region under normal forward-active operational mode. 30

4-1 Theoretical calculated built-in voltage as a function of doping concentration in epilayer (for a fixed base doping) for the different SiGe HBTs. 36
4-2 Measured (symbols) and simulated (solid lines) base current as a function of collector-base voltage (V_{cb}) at seven different temperatures $T \in \{-25, 0, 25, 50, 75, 100, 125\}$ °C for HVCOM (NPN) SiGe HBT. (a) presents the local avalanche current model results with parameters W_{AVL} = 576.0 nm and V_{AVL} = 2.0 V. (b) presents the non-local avalanche current model results with W_{AVL} = 427 nm, V_{AVL}= 0.75 V, L_{AVL} = 28.3 nm, and A_{LAVL} = −1.1 as parameter values. 38
4-3 Measured (symbols) and simulated (solid lines) base current as a function of collector-base voltage (V_{cb}) at five different temperatures $T \in \{25, 50, 75, 100, 125\}$ °C for HS SiGe HBT. (a) presents the local avalanche current model results with parameters W_{AVL} = 128.10 nm and V_{AVL} = 0.15 V. (b) presents the non-local avalanche current model results with parameters W_{AVL} = 104.0 nm, V_{AVL} = 0.69 V, L_{AVL} = 62.34 nm, and A_{LAVL} = −1.2 as model parameter values. 40
4-4 Measured (symbols) and simulated (solid lines) base current as a function of collector-base voltage (V_{cb}) at five different temperatures $T \in \{25, 50, 75, 100, 125\}$°C for RF SiGe HBT. (a) presents the local avalanche model results with parameters W_{AVL} = 261.0 nm and V_{AVL} = 0.80 V. (b) presents the non-local avalanche model results with W_{AVL} = 229.9 nm, V_{AVL} = 0.87 V, L_{AVL}= 27.0 nm, and A_{LAVL} = −0.48 as parameter values. 42
4-5 Measured (symbols) and simulated (solid lines) base current as a function of collector-base voltage (V_{cb}) at five different temperatures $T \in \{25, 50, 75, 100, 125\}$ °C for HVCOM (PNP) transistor. (a) presents the local avalanche model results with parameters W_{AVL} = 272.1 nm and V_{AVL} = 0.89 V. (b) presents the non-local avalanche model results with W_{AVL} = 256.3 nm, V_{AVL} = 0.9 V, L_{AVL} = 35 nm, and A_{LAVL} = −1.2 as parameter values. 44

A-1 Measured (symbols) and simulated (solid lines) base-emitter depletion capacitance (C_{be}) as a function of base-emitter voltage (V_{be}) and temperature $T \in \{-25, 0, 25, 50, 75, 100, 125\}$ °C. 52
A-2 Measured (symbols) and simulated (solid lines) base-collector depletion capacitance (C_{bc}) as a function of base-collector voltage (V_{bc}) and temperature $T \in \{-25, 0, 25, 50, 75, 100, 125\}$ °C. 52
A-3 Measured (symbols) and simulated (solid lines) base current (I_b) as a function of base-emitter voltage (V_{be}) and temperature $T \in \{-25, 0, 25, 50, 75, 100, 125\}$ °C. 53
A-4 Measured (symbols) and simulated (solid lines) collector current (I_c) as a function of base-emitter voltage (V_{be}) and temperature $T \in \{-25, 0, 25, 50, 75, 100, 125\}$ °C. 54
A-5 Measured (symbols) and simulated (solid lines) base current (I_b) as a function of base-collector voltage (V_{bc}) and temperature $T \in \{-25, 0, 25, 50, 75, 100, 125\}$ °C. 55
A-6 Measured (symbols) and simulated (solid lines) emitter current (I_e) as a function of base-collector voltage (V_{bc}) and temperature $T \in \{-25, 0, 25, 50, 75, 100, 125\}$ °C. 55

A-7 Measured (symbols) and simulated (solid lines) collector current (I_c) as a function of collector-base voltage (V_{cb}) and temperature $T \in \{-25, 0, 25, 50, 75, 100, 125\}$ °C. 56
A-8 Measured (symbols) and simulated (solid lines) collector current (I_c) as a function of collector-emitter voltage (V_{ce}) at temperature (T_3)°C. 57
A-9 Measured (symbols) and simulated (solid lines) base-emitter voltage (V_{be}) as a function of collector-emitter voltage (V_{ce}) at temperature (T_3) °C. 57
A-10 Measured (symbols) and simulated (solid lines) base-emitter depletion capacitance (C_{be}) as a function of base-emitter voltage (V_{be}) and temperature $T \in \{25, 50, 75, 100, 125\}$ °C. 59
A-11 Measured (symbols) and simulated (solid lines) base-collector depletion capacitance (C_{bc}) as a function of base-collector voltage (V_{bc}) and temperature $T \in \{25, 50, 75, 100, 125\}$ °C. 59
A-12 Measured (symbols) and simulated (solid lines) base current (I_b) as a function of base-emitter voltage (V_{be}) and temperature $T \in \{25, 50, 75, 100, 125\}$ °C. . 60
A-13 Measured (symbols) and simulated (solid lines) collector current (I_c) as a function of base-emitter voltage (V_{be}) and temperature $T \in \{25, 50, 75, 100, 125\}$ °C. 61
A-14 Measured (symbols) and simulated (solid lines) emitter current (I_e) as a function of base-collector voltage (V_{bc}) and temperature $T \in \{25, 50, 75, 100, 125\}$ °C. 62
A-15 Measured (symbols) and simulated (solid lines) base current (I_b) as a function of base-collector voltage (V_{bc}) and temperature $T \in \{25, 50, 75, 100, 125\}$ °C. 62
A-16 Measured (symbols) and simulated (solid lines) collector current (I_c) as a function of collector-base voltage (V_{cb}) and temperature $T \in \{25, 50, 75, 100, 125\}$ °C. 63
A-17 Measured (symbols) and simulated (solid lines) collector current (I_c) as a function of collector-emitter voltage (V_{ce}) at temperature T_3=25°C. 64
A-18 Measured (symbols) and simulated (solid lines) base-emitter voltage (V_{be}) as a function of collector-emitter voltage (V_{ce}) at temperature T_3=25°C. . . . 64

List of Tables

2.1 Different HBT technologies, Manufacturer and acronyms for the measured SiGe HBT. 8
2.2 Properties of the measured SiGe HBTs at 25°C. 8
2.3 Temperatures at which measurements were carried out on different SiGe HBTs. 8
2.4 Relevant Mextram parameter extraction procedure for the parameters relevant in avalanche current simulation. 10

4.1 Relaxation length(L_{AVL}), effective width of the epilayer for avalanche current (V_{AVL}), voltage describing the curvature of avalanche current (W_{AVL}), temperature coefficient of relaxation length (A_{LAVL}), and root-mean-square (RMS) error values extracted for the SiGe HBT technologies. 34
4.2 Mean (μ) value ,standard deviation (σ) 37
4.3 Parameter values for different transistor technologies extracted for the nonlocal avalanche model. 45

CHAPTER 1

Introduction

Modern communication gadets operating at high frequencies requires faster electronic devices, and such electronic devices demand higher doping concentrations, which results into reduced breakdown voltage. Modeling the breakdown phenomena in today's high-speed circuit design is becoming more important and challenging. To fully exploit the operational capability of Si and SiGe transistors, an accurate modeling of the breakdown phenomena is important for electronic circuit design.

1.1 Trade-off Between Transistor Speed and Breakdown

The increase in doping concentration of bipolar transistors leads to an increase in electric field across the transistor junction. This increase in electric causes an increase in impact ionization and avalanche effects, and hence a reduction in the breakdown voltage. The demand for high speed devices in modern communication requires the devices to operate at high frequencies. This further demands for higher unity current gain frequency f_T and maximum unity power gain frequency f_{max}. Higher values of f_T and f_{max} are obtained by high doping concentrations in the transistor and therefore reduced breakdown voltage. The higher breakdown voltage of a transistor is a crucial design factor for designing power amplifiers in wireless transmitters. The higher breakdown voltage is also one of the top priorities in the automotive industry. In high-speed silicon technologies the f_T can be increased by increasing the doping concentration in collector epilayer or by decreasing the thickness of collector epilayer, both of which delay the onset of Kirk effect. The increase in collector doping concentration leads increase in base-width modulation and impact ionization. The increase in impact ionization lowers the breakdown voltage. The reduction in the epilayer thickness also causes an increase in the impact ionization due to higher electric field from the same voltage across a shorter distance. The trade-off between f_T and the breakdown voltage is also referred as 'Johnson Limit' [3],

which states that, due to the material limitations in carrier velocity and avalanche generation, the product of cut-off frequency and collector-emitter breakdown voltage with open base (BV_{CEO}) should be relatively constant. This fundamental reciprocal relationship between peak f_T and BV_{CEO} for SiGe HBTs and SiGeC HBT technologies is shown in the Figure 1-1.

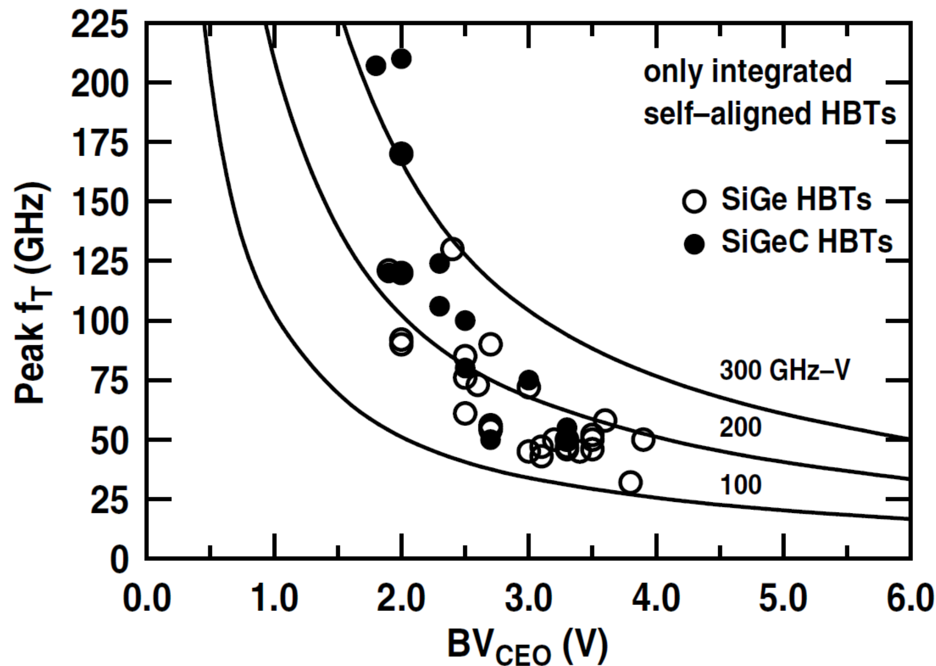

Figure 1-1: The cut-off frequency as a function of collector-to-emitter breakdown voltage with open base for integrated self-aligned SiGe HBT and SiGeC HBT technologies [1].

Most published SiGe HBT results are centered upon an $f_T \times BV_{CEO}$ of about 200 GHz-V which is slightly higher than the original 'Johnson Limit' for Si of 170 GHz-V. Most recent results suggest that the higher values of the $f_T \times BV_{CEO}$ product are attainable as SiGe technologies evolve. On-going vertical profile scaling reduces the carrier transit times of SiGe HBTs. Together with the graded Ge profile in SiGe HBTs leads to increase in f_T which degrades BV_{CEO} due to the increase in the current gain.
In contrast to this increase in f_T by postponing the Kirk effect, all degrades the base-collector junction breakdown voltage BV_{CEO} due to increase of the built-in electric field caused by the increase of collector doping concentration. This can also be observed from the Figure 1-1, for higher cut-off frequencies, the breakdown voltages are low. This limitation has forced circuit designers to design electronic circuits that work beyond the breakdown voltage (usually BV_{CEO}). For circuit designers it is very important to know the limit a circuit can be biased beyond BV_{CEO}. This limit is usually defined as the safe area of operation. In order to accurately define the safe area of operation, clear understanding and accurate modeling of breakdown mechanisms like tunneling breakdown and avalanche breakdown is required. This thesis focuses only on the avalanche breakdown, therefore only the avalanche breakdown will be discussed in this work.

1.2 Avalanche Breakdown in Bipolar Junction Transistors

Avalanche breakdown in bipolar junction transistors originates from impact ionization across the collector-base junction in the forward operation mode of transistor. Under large base-collector reverse voltage charge carriers in the base-collector space charge region gain enough kinetic energy under the influence of high electric field so that a collision with the semiconductor atom can break the bond between the atom and one of the bond electron, causes a valence electron to move up into the conduction band. At the same time a hole is generated, therefore in the process of impact ionization, the electric field is responsible for transferring energy to drift electrons, but it is the accumulated energy of electrons that is responsible for the impact ionization.
Impact ionization is one of the most common breakdown mechanism in practical bipolar transistors. During the impact ionization, the original carrier and the electron and hole generated are accelerated in opposite directions by the electric field and in turn are able to produced further electron-hole pairs by impact ionization. This process known as avalanche multiplication, rapidly leads to generation of large number of carriers and hence a large current [4]. For avalanche multiplication to occur, a critical electric field E_{crit} must be established across the reverse-biased junction. Since the depletion width depends on the doping concentration, it is clear that the breakdown voltage BV_{CEO} will also depend on the doping concentration. For example, for the one-sided step base-collector junction, the breakdown voltage is given by [5]:

$$BV_{\mathrm{CEO}} = \frac{\varepsilon_o \varepsilon_r E_{crit}^2}{2qN_{\mathrm{epi}}}, \tag{1.1}$$

where N_{epi} is the doping concentration of lightly doped epilayer, ε_o and ε_r are permittivity of free space and relative permittivity of silicon, respectively. If E_{crit}, assumed constant, Eq (1.1) would indicate that the breakdown voltage is inversely proportional to the epilayer doping concentration. But in practice E_{crit} varies slightly with the doping concentration.
A number of technology computer-aided design (TCAD) models have been developed in order to study the breakdown phenomena. The fast models that are used for the integrated circuit design are compact models which will be discussed in the next section.

1.3 Compact Modeling in Bipolar Junction Transistors

Compact transistor models are vital components of circuit simulations as they define the terminal characteristics of transistors. Such models consists of a combination of circuit elements such as resistors, capacitors, and current generators together with equations defining the behavior of the transistor. In devising a compact transistor model, an accurate description of the terminal characteristics is more important than a rigorous description of the device physics. Nevertheless, models that are based on the physics of the device do provide a better understanding, and can generally be implemented using fewer model parameters [4]. Other reasons for developing compact models that are physics based may include: possibilities to carry out data extrapolation (i.e., prediction of device characteristics beyond the ranges

in which measurements have been taken), enabling - e.g. prediction of noise without need for measured noise data, and extraction of model parameters that have got a physical interpretation (these parameters are scalable as a function of device temperature and geometry and can also allow modeling of statistical spread by means of specification of the statistical distribution of parameter values). For these reasons, most circuit simulators use compact transistor models that are to a first order physics-based, although second-order effects are often described using simple empirical expressions. Computational time is of paramount importance, since this provides a limit to the size of circuit that can be simulated.
The need for shorter simulation times is the primary reason that compact models are used for circuit simulation in preference to full numerical device simulation [4]. Compact transistor models provides an interface between process engineers, device engineers, and integrated circuit designers. Circuit designers need to be familiar with the compact models, because the accuracy of their circuit simulations depend critically on the accuracy of the transistor compact model and the corresponding input parameters. Similarly, process and device engineers need to have some knowledge of the transistor models, because the transistor and process design need to be optimized to give optimum circuit performance [4].
The Eber-Moll [6] and Gummel-Poon (GP) model were the initial compact bipolar transistor models and they are used widely available computer-aided circuit design programs such as SPICE. These transistor models are now incapable of describing important physical phenomena in the modern transistor technologies. For modern transistor technologies there is a requirement for more capable compact models which can address vital effects such as avalanche breakdown, quasi-saturation, Kirk effect, and self-heating. More recent advanced compact models such as Most EXquisite TRAnsistor Model (MEXTRAM) [2], HIgh-CUrrent Model (HICUM) [7], and Vertical Bipolar InterCompany (VBIC) [8] captures such physical phenomena. Presently these are the most advanced compact models for bipolar junction transistors.
The avalanche modeling in Mextram, Hicum, and Vbic are similar to a large extent. The only difference between these compact models (Vbic and Hicum) and Mextram are, Hicum and Vbic compact models do not consider the case where for higher current densities, the maximum value of the electric field occurs at the epilayer-buried layer interface instead of base-collector junction. The Mextram model can describes avalanche for decreasing effective epilayer due to base-widening and the collector current spreading effect by extended avalanching modeling.
Mextram model is a widely used vertical bipolar transistor simulation and it supports the design of bipolar transistor circuits and silicon-germanium based process technologies. Mextram was been selected by the Compact Model Coalition (CMC) [9] as a world standard bipolar transistor compact model for the semiconductor industry. Mextram is developed and supported at Delft University of Technology. Mextram 504.11.0 is the current version released in December 2012. The complete Mextram model definition can be refereed from Mextram web-site [2].

1.4 Research Goals and Objectives

The avalanche current in different compact models is modeled using a conventional impact ionization approach. This conventional impact ionization approach employs the local-electric field and assumes that charge carriers are energized instantaneously to the steady-state kinetic energy corresponding to the local-electric field intensity.
From the extensive DC measurements and Mextram model simulations that was carried out on several modern SiGe HBT technologies over temperature, deviations between the measurement and Mextram simulation were observed. The conventional avalanche modeling approach in Mextram model produced the observed deviations between the measurement and simulation results over temperature.
In spatial electric field, the charge carrier energy lags the electric field due to presence of finite energy relaxation time [10]. Currently, the non-local impact ionization is modeled in the TCAD device simulations. As mentioned in [11], in compact models the non-local effects can be compensated by the extracted parameter values and good fits may be achieved over the desired region. From the extensive DC measurements and Mextram simulations such good fits for the avalanche current over temperature were not achieved. Also, the extracted Mextram parameter values were not physical.
In order to address the issues mentioned above and to accurately describe the avalanche current over temperature in Mextram compact model, the non-local avalanche effects should be taken into account. The carriers impact ionization process should be described in terms of the carrier energy (carrier temperature) instead of the local electric field. Using this approach the non-local avalanche model was developed and implemented in Mextram at Delft University of Technology. The motivation behind this thesis is to study avalanche current in Mextram as a function of temperature and bias (in weak avalanche region) and also to experimentally verify the implemented non-local avalanche Mextram model. The key research objectives that address the key research goals are mentioned below:

- Carrying out DC measurements on different SiGe HBT technologies over temperature and bias.

- Studying and analyzing the current status of avalanche current model in Mextram compact model.

- Understanding the non-local avalanche current model that is implemented in Mextram compact model.

- Verifying the implemented non-local avalanche current in Mextram using temperature measurement on different SiGe HBT technologies.

- Investigating the temperature scaling of weak non-avalanche current model.

- Determining the accuracy of extracted non-local avalanche model parameter values in Mextram.

1.5 Thesis Organization

The presented work focuses on verification of the non-local avalanche current model implemented in Mextram compact model and is organized in following chapters.

Chapter 2 presents the DC measurement and Mextram simulation results carried on several industrial SiGe HBT technologies over different temperatures. The measured results are compared with corresponding Mextram simulation results as a function of temperature for the measured SiGe HBT technologies. The incapabilities of Mextram 504.11.0 to describe accurately the avalanche current as a function of temperature are demonstrated in this chapter. Also the extraction procedure for the model parameters relevant for describing the avalanche current in Mextram is described.

Chapter 3 investigates the current status of the avalanche current model in Mextram. Later, in the chapter the physical formulation of the non-local avalanche current model in Mextram is presented. The concept of relaxation length based on energy balance equation is introduced in the non-local avalanche model. The temperature scaling rule for relaxation length used in the implemented non-local avalanche is also presented.

Chapter 4 presents the parameter extraction procedure for the non-local avalanche current model parameters in Mextram. In addition, the experimental verification of the non-local avalanche current model over temperature on measured SiGe HBTs is also presented. The accuracy of the extracted parameters in Mextram compact model is also discussed.

Chapter 5 presents the main conclusions of the thesis and provides several recommendations for the future work.

CHAPTER 2

DC Measurements and Mextram Simulation Results

In this chapter the direct current (DC) measurements over temperature and corresponding Mextram model simulations carried out on different modern SiGe HBTs are presented. The Mextram model parameter extraction procedure is also presented. The main goal of this chapter is to study the temperature dependence of the avalanche current for different industrial SiGe HBTs. The measured and Mextram simulated results are compared in order to analyze the setbacks in the Mextram avalanche current model.

2.1 DC Measurement Set-up

The temperature dependence of the avalanche current in Mextram model is studied and analyzed by means of Forward Early DC measurements carried out at different temperatures. In order to test the Mextram's avalanche model, more basic current characteristics must also be modeled adequately and the corresponding model parameters have to be extracted. This is due to the fact that in Mextram, the main transistor current is an input of the avalanche model (as will be elaborated in Chapter 3). Therefore, other DC measurements over temperature such as depletion capacitance, Forward Gummel, Reverse Gummel, and Output characteristics were also carried out and used to extract all relevant model parameters. All these measurements were carried out on different industrial SiGe HBTs. The SiGe HBTs used for the measurements are: high voltage, typical industrial (both NPN & PNP HBTs), high-speed QUBiC4X (NPN) BNX-type process [12] by NXP Semiconductors, and ADI (NPN) by Analog Devices Inc. For convenience, acronyms will be used for these measured SiGe HBTs in rest of the thesis as presented in Table 2.1.
The important properties of different measured SiGe HBTs are summarized in Table 2.2.

From Table 2.2, it can be seen that the HS SiGe HBT has the highest cut-off frequency (f_T =

Table 2.1: Different HBT technologies, Manufacturer and acronyms for the measured SiGe HBT.

HBT Technology	Manufacturer	Acronym
Typical Industrial (NPN and PNP)		HVCOM
QUBiC4X	NXP Semiconductors	HS
ADI	Analog Devices Inc	RFCOM

Table 2.2: Properties of the measured SiGe HBTs at 25°C.

HBT Technology	Area (μm^2)	BV$_{CEO}$ (V) (at V$_{BE}$ = 0.65V)	f_T (GHz)	f_{max} (GHz)
HVCOM (NPN)	0.40 × 3.20	5.00	25	40
HS (NPN)	0.35 × 0.27	1.32	137	180
RFCOM (NPN)	0.35 × 5.20	2.63	50	65
HVCOM (PNP)	0.40 × 3.20	4.95	28	35

137 GHz) and lowest collector-emitter breakdown voltage with an open base (BV$_{CEO}$ = 1.32V). Such a transistor has a short epilayer that is highly doped and according to device physics it is expected that the impact ionization in such transistor will be high. The HVCOM (NPN) SiGe HBT has largest breakdown voltage (BV$_{CEO}$ = 5.00V) and lowest cut-off frequency (f_T = 25 GHz). This implies that this transistor has low doping concentration with long epilayer. Low impact ionization is expected in a such transistor. Hence, due to low doping concentration the impact ionization will be lower. In Table 2.3, the temperatures at which measurements were carried on different SiGe HBTs are presented.

Table 2.3: Temperatures at which measurements were carried out on different SiGe HBTs.

Temperature	(°C)
T_1	−25
T_2	0
T_3	25
T_4	50
T_5	75
T_6	100
T_7	125

Mextram model parameters were extracted for each measured SiGe HBT using the DC measurements. The parameter extraction procedure for the Mextram model parameters that are relevant for the avalanche current simulation is discussed in the next section.

2.2 Parameter Extraction in Mextram Compact Model

Parameter extraction is an important concept in compact modeling. Reliable circuit simulations involving compact models not only depends on the accurate description of various physical phenomena, but also depends on reliable, robust, and unambiguous parameter extraction procedure. A poor quality of extracted parameter set will result in unreliable circuit simulation results. Hence, the predication of circuit simulations involving compact models like Mextram strongly depends on the quality of extracted parameter values. The parameter extraction procedure in Mextram model for the parameters associated with the avalanche current simulation is presented below.

The parameter extraction begins by employing the Mextram model (coded in Verilog-A language) within an Integrated Circuit Characterization and Analysis Program (IC-CAP) [13] environment along with a circuit simulator Advanced Design Systems (ADS) (by Agilent technologies). The Mextram model parameters are extracted in two categories. In first category, the electrical parameters of Mextram model are extracted at reference temperature (here $T_{ref} = 25\ °C$). In second category, by employing different temperature scaling rules for the electrical parameters, the temperature parameters are extracted over different temperatures. In Table 2.4, the extraction sequence for the relevant electrical and temperature parameters in the Mextram model are presented. It should be noted that all these parameters are required for simulating the avalanche current in the Mextram model.

Table 2.4: Relevant Mextram parameter extraction procedure for the parameters relevant in avalanche current simulation.

Measurement Type	Measured Data	Measurement Regime	Extraction Region	Extracted Parameter(s)
Base-Emitter depletion capacitance	C_{BE} [V_{BE}, T]	V_{CB} = 0V, T = T_{min}....T_{max}	Low V_{BE}, T = T_{min}....T_{max}	C_{j_E}, V_{d_E}, p_E
Base-Collector depletion capacitance	C_{BC} [V_{BC}, T]	V_{BE} = 0V, T = T_{min}....T_{max}	Low V_{BC}, T = T_{min}....T_{max}	C_{j_C}, V_{d_C}, p_C, X_P
Substrate-Collector depletion capacitance	C_{SC} [V_{BC}, T]	V_{BE} = 0V T = T_{min}....T_{max}	Low V_{BC}, T = T_{min}....T_{max}	C_{j_S},V_{d_S}, p_S
Forward Gummel	I_C [V_{BE}, T_{ref}]	V_{CB} = 0V, T = T_{ref}	Low forward bias V_{BE}, ideal region	I_S, V_{er}
	I_B [V_{BE}, T_{ref}]	V_{CB} = 0V, T = T_{ref}	Low forward bias V_{BE}, ideal region	β_f, XI_{BI}
	I_B [V_{BE}, T_{ref}]	V_{CB} = 0V, T = T_{ref}	Low forward bias V_{BE}, non-ideal region	I_{Bf}, m_{Lf}
Reverse Gummel	I_B [V_{BC}, T_{ref}]	V_{EB} = 0V, T = T_{ref}	Low forward bias V_{BC}, ideal region	β_{ri}
	I_B [V_{CB}, T_{ref}]	V_{EB} = 0V, T = T_{ref}	Low forward bias V_{BC}, non-ideal region	I_{Br}, V_{Lr}
	I_S [V_{CB}, T_{ref}]	V_{EB} = 0V, T = T_{ref}	Low forward bias V_{BC}, ideal region	I_{Ss}, I_{CSs}
Forward Early	I_C [V_{CB}, T_{ref}]	V_{BE} = const, T = T_{ref}	Low V_{CB} bias, non-avalanche region	V_{ef}
	I_B [V_{CB}, T_{ref}]	V_{BE} = const, T = T_{ref}	Medium V_{CB} bias, weak-avalanche region	W_{avl}, V_{avl}
Forward Gummel	I_B [V_{BE}, T_{ref}]	V_{BC} = 0V, T = T_{ref}	High forward bias V_{BE}, high-current region	R_E
Reverse Gummel	I_S [V_{BC}, T_{ref}]	V_{BE} = 0V, T = T_{ref}	High forward bias V_{BC}, high-current region	I_{ks}

Measurement Type	**Measured Data**	**Measurement Regime**	**Extraction Region**	**Extracted Parameter(s)**
Forward Gummel	I_C [V_{BE}, T]	V_{BC} = 0V, T = T_{min}....T_{max}	Low forward bias V_{BE}, ideal region, T = T_{min}....T_{max}	V_{gB}
	I_B [V_{BE},T]	V_{BC} = 0V, T = T_{min}....T_{max}	Low forward bias V_{BE}, ideal region, T = T_{min}....T_{max}	$dV_{g\beta f}$
	I_B [V_{BE},T]	V_{BC} = 0V, T = T_{min}....T_{max}	Low forward bias V_{BE} non-ideal region, T = T_{min}....T_{max}	V_{gj}
Reverse Gummel	I_B [V_{BC},T]	V_{EB} = 0V, T = T_{min}....T_{max}	Low forward bias V_{BC}, ideal region, T = T_{min}....T_{max}	$dV_{g\beta r}$
	I_B [V_{BC},T]	V_{EB} = 0V, T = T_{min}....T_{max}	Low forward bias V_{BC} non-ideal region, T = T_{min}....T_{max}	V_{gC}
	I_S [V_{BC},T]	V_{EB} = 0V, T = T_{min}....T_{max}	Low forward bias V_{BC}, ideal region, T = T_{min}....T_{max}	V_{gS},
Output Characteristics	I_S [V_{CE}, T_{ref}]	I_B = *fixed*, T = T_{ref}	Low forward bias V_{CE} quasi-saturation region	R_{Cc}, R_{Cblx}, R_{Cbli}
	V_{BE} [V_{CE}, T_{ref}]	I_B = *fixed*, T = T_{ref}	Medium V_{CE}, non-avalanche region	R_{th}
	I_C [V_{CE}, T_{ref}]	I_B = *fixed*, T = T_{ref}	Medium V_{CE}, non-avalanche region	I_k

The relevant Mextram parameters for describing the avalanche current as a function of temperature were extracted in a chronological order as described in Table 2.4. As mentioned before, the electrical parameters are extracted first at a reference temperature (represented by T_{ref} in Table 2.4). The depletion capacitance parameters are extracted first from the capacitance measurements as a function of temperature at low bias.
The collector-emitter saturation current parameter I_s and Reverse Early voltage parameter V_{er} are extracted from the collector current (I_C) in the ideal region of the Forward-Gummel measurements at T_{ref}. Using the same Forward-Gummel measurements the forward current gain parameter β_f, saturation current of the non-ideal forward base current parameter I_{Bf},

part of ideal base current that belongs to the side wall parameter XI_{BI}, and non-ideality factor of the non-ideal forward base current M_{LF} are extracted from, the ideal and non-ideal parts of base current at T_{ref}.
The reverse current gain parameter β_{ri} is extracted at T_{ref} from the base current (I_B) in ideal region of Reverse-Gummel measurements. Using the same measurements other parameters i.e., I_{Br} and V_{Lr} are extracted from the non-ideal region I_B while parameters I_{Ss}, I_{CSs}, and I_{KS} are extracted from the Reverse-Gummel substrate current (I_s) over the ideal region.
The Forward Early voltage parameter (V_{ef}) is extracted from I_C over non-avalanche region of the Forward-Early measurements at T_{ref}. The avalanche parameters W_{avl} and V_{avl} are extracted from I_B corresponding to the Forward Early measurements over the weak avalanche region. After extracting all the relevant electrical parameters, the relevant temperature parameters in Mextram model are also extracted.
The band-gap temperature parameters V_{gB}, $dV_{\beta f}$, and V_{gj} are extracted from the Forward-Gummel temperature measurements. The other band-gap temperature parameters $dV_{\beta r}$, V_{gc}, and V_{gs} are extracted from the Reverse-Gummel temperature measurements.
After extracting all relevant temperature parameters, the parameters R_{Cc}, R_{Cblx}, R_{Cbli}, R_{th}, and I_k are extracted at T_{ref} from the various regions of the Output characteristics measurements. Since these parameters are high-current parameters, they are extracted after extracting the temperature parameters in order to take self-heating into account. In general, the parameter extraction is a cyclic process and extraction procedure is repeated several times in order to get an optimal parameter set.
In order to study and analyze the temperature dependence of the avalanche current in Mextram model, the Forward Early measurements and simulations are employed and the corresponding results are presented for the different SiGe HBT technologies in the next section. The measurements and simulation results for the Forward-Gummel, Reverse-Gummel, capacitance measurement and Output characteristics are presented in Appendix A. Note that in Appendix A only results for HVCOM (NPN & PNP) are presented. The results for other SiGe HBTs are left out as they follow the same sequence.

2.3 Analysis of the Temperature Dependence of Avalanche Current in Mextram Model

The Forward Early measurements are used to define the avalanche current were carried on different SiGe HBT technologies at a constant applied base-emitter voltage (V_{BE} = 0.65V) and variable collector-base voltage (V_{cb}) at different temperatures (shown in Table 2.3). In order to avoid high injection effects such as self-heating and quasi-saturation which can make the analysis of avalanche current complex a relatively small V_{BE} (0.65V) was chosen during the measurements. The current Mextram (version 504.11.0) model addresses only the weak avalanche current i.e., the charge carriers generated in the process of impact ionization do not generate extra carriers and the generated avalanche current is smaller than the collector current. Therefore, the avalanche current studied in this thesis is the weak avalanche (neglecting the strong avalanche current).

The avalanche current parameters i.e., W_{avl} and V_{avl} were extracted as described in Section 2.2. During the extraction of these avalanche parameters, a flag EXAVL (EXtended AVaLanche) is set to zero (i.e., EXAVL = 0). The measured and Mextram simulated results for the avalanche current as a function of temperature and bias for all the measured SiGe HBT technologies are presented in the next subsections.

2.3.1 Measured and Simulated Base Current for HVCOM (NPN) SiGe HBT

The measured (symbols) and simulated (solid lines) results for the base current as a function of temperature and collector-base voltage (V_{cb}) for HVCOM (NPN) SiGe HBT are presented in Figure 2-1.

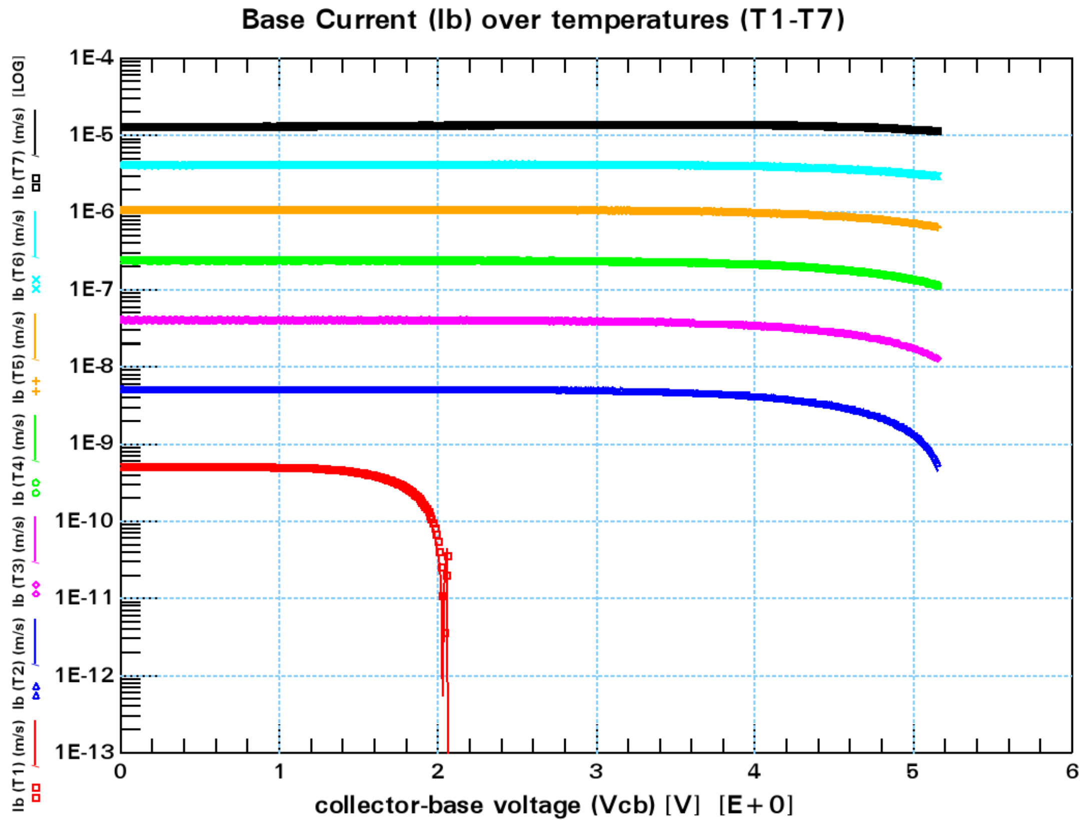

Figure 2-1: Measured (symbols) and simulated (solid lines) base current as a function of collector-base voltage (V_{cb}) and device temperature for HVCOM (NPN) SiGe HBT. Here, $V_{BE} = 0.65V$ and $T \in \{-25, 0, 25, 50, 75, 100, 125\}$ °C. Due to the perfect fit, the simulation results overlaps with the measurement results so they are not visible.

From Figure 2-1 an excellent agreement is observed between the measured and simulated base current over all temperatures and bias regions (non avalanche and weak avalanche region). Note that the I_b (vertical axis) is in logarithmic scale as in all other results that will be presented in this thesis.

2.3.2 Measured and Simulated Base Current for HS (NPN) SiGe HBT

For the HS SiGe HBT, the measured (symbols) and simulated (solid lines) results for the base current as a function of temperature and collector-base voltage (V_{cb}) are presented in Figure 2-2.

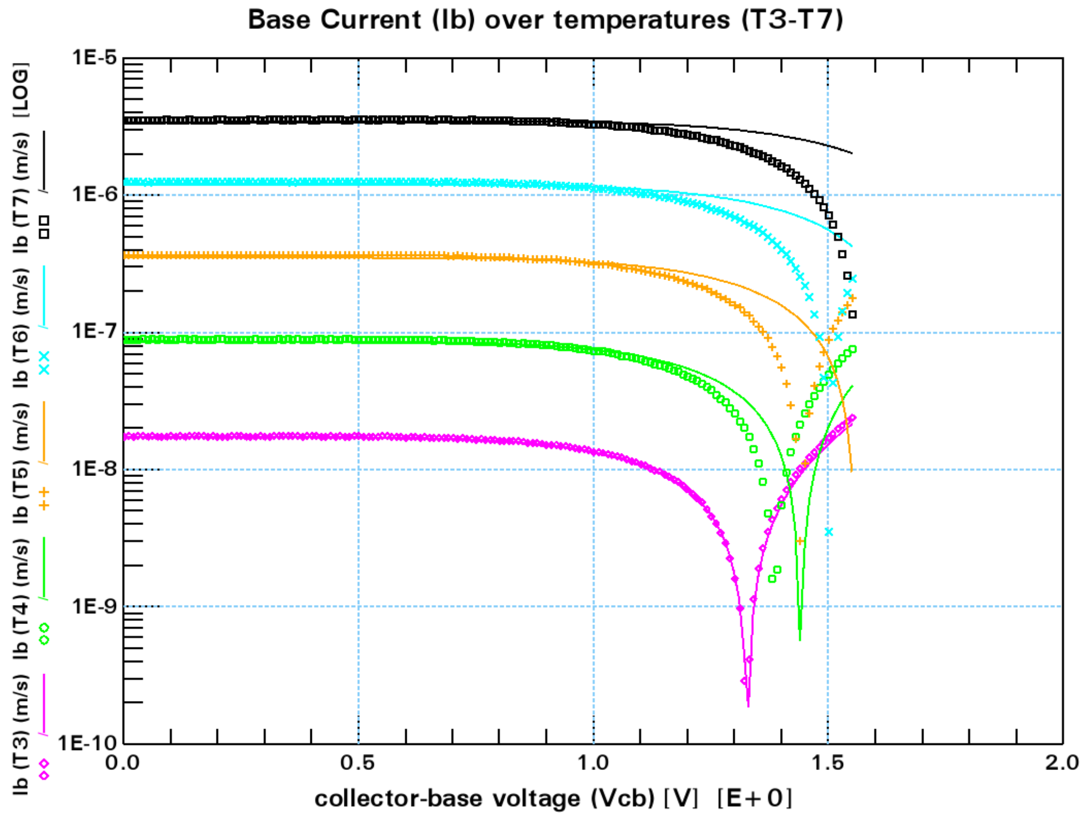

Figure 2-2: Measured (symbols) and simulated (solid lines) base current as a function of collector-base voltage (V_{cb}) and device temperature for HS (NPN) SiGe HBT. Here, V_{BE} = 0.65V and T $\in$ $\{25, 50, 75, 100, 125\}$ °C.

From Figure 2-2, large deviations between the measured and simulated base current as a function of temperature are observed over the *weak avalanche* region (V_{cb} >1.0V). Since, the avalanche current was optimized first at reference temperature (i.e., at T_3 = 25 °C), an excellent fit is observed corresponding to this temperature. For other temperatures i.e., T_4, T_5, T_6, and T_7, an increase in deviations between the measured and simulated base current with temperature is observed over the *weak avalanche* region. These results suggests, that the current Mextram avalanche model is insufficient to define the avalanche current as a function of temperature over the *weak avalanche* region. This will be addressed later in this thesis.

2.3.3 Measured and Simulated Base Current for RFCOM (NPN) SiGe HBT

The measured (symbols) and simulated (solid lines) base current as a function of temperature and collector-base voltage (V_{cb}) for RFCOM SiGe HBT are presented in Figure 2-3.

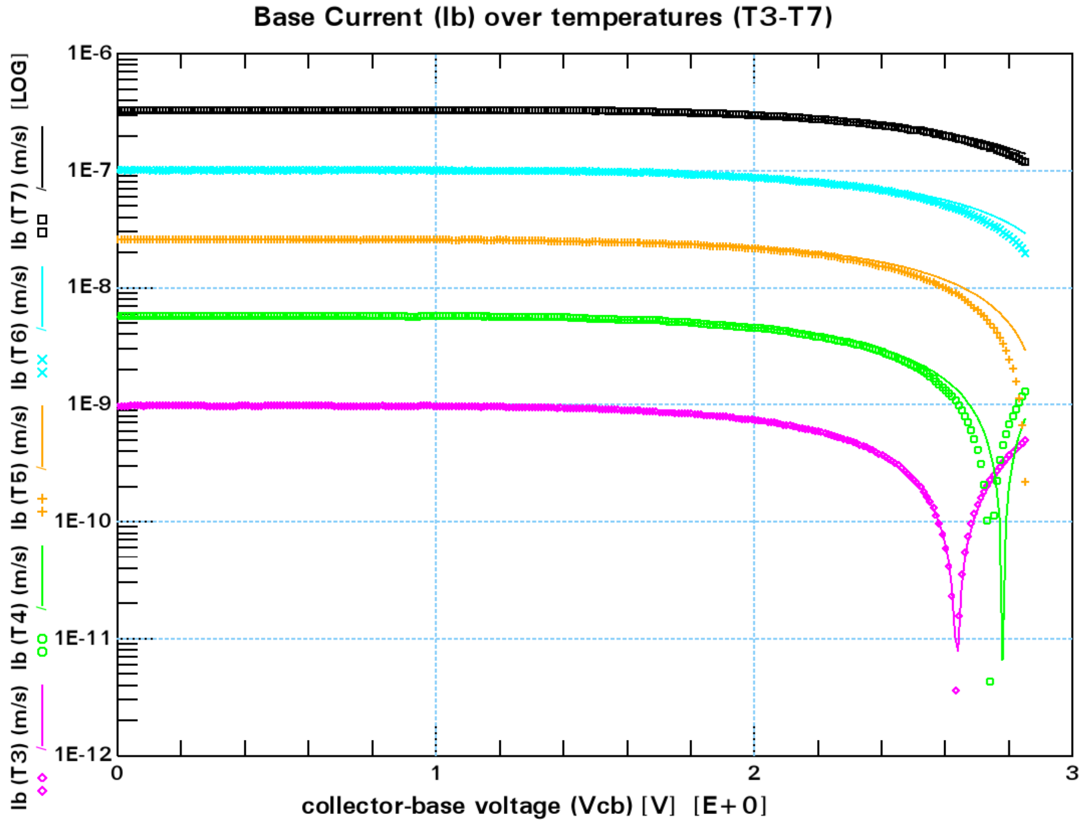

Figure 2-3: Measured (symbols) and simulated (solid lines) base current as a function of collector-base voltage (V_{cb}) and device temperature for RFCOM (NPN) SiGe HBT. Here, V_{BE} = 0.65V and T $\in$ $\{25, 50, 75, 100, 125\}$ °C.

It can be observed from Figure 2-3, that the simulated I_b does not fit the measured base current over different temperatures in the weak avalanche region (V_{cb} >2.0V). The simulated I_b shows deviations from the measured I_b at temperatures T_4, T_5, T_6, and T_7 over the *weak avalanche* region. The deviations between the measured and simulated I_b as a function of temperature for RFCOM SiGe HBT are less than those observed in HS SiGe HBT (see Figure 2-2).

2.3.4 Measured and Simulated Base Current for HVCOM (PNP) SiGe HBT

For the HVCOM (PNP) SiGe HBT, the measured (symbols) and simulated (solid lines) results of the base current (I_b) as a function of temperature and collector-base voltage (V_{cb}) is presented in the Figure 2-4.
From this figure, a misfit between the measured and the simulated I_b as a function of temperature is observed over the *weak avalanche* region (V_{cb} >3.5V). These deviations in the I_b for HVCOM (PNP) SiGe HBT are smaller compared to those observed in the HS SiGe HBT (see Figure 2-2).

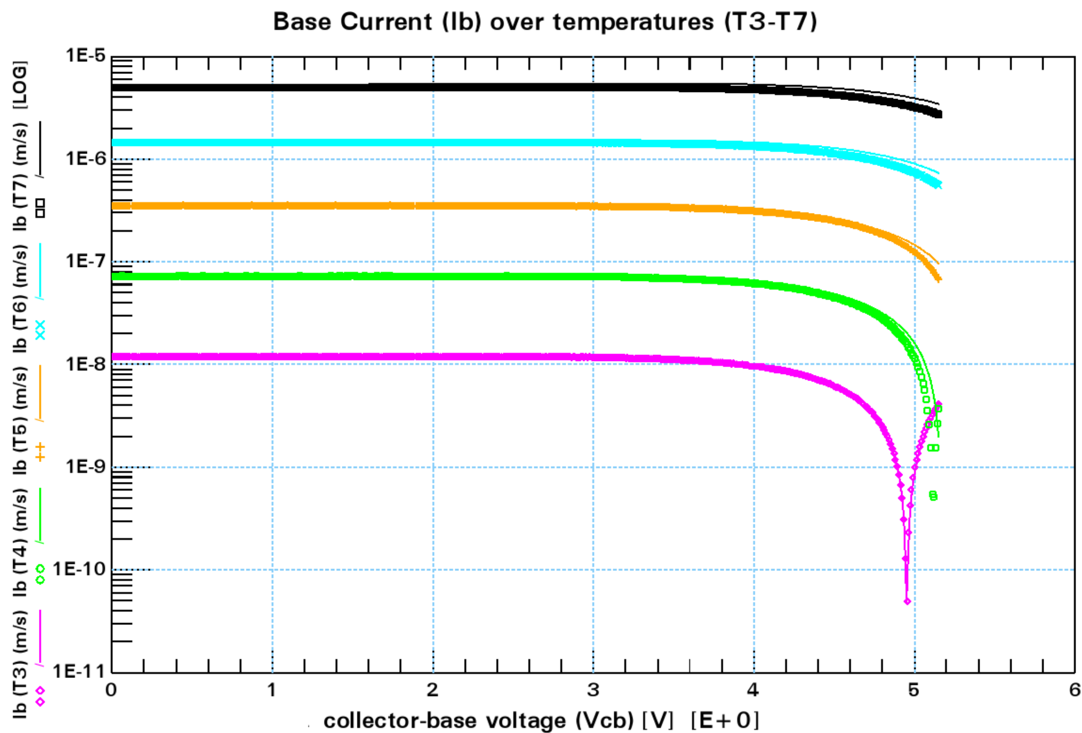

Figure 2-4: Measured (symbols) and simulated (solid lines) base current as a function of collector-base voltage (V_{cb}) and device temperature for HVCOM (PNP) SiGe HBT. Here, V_{BE} = 0.65V and T $\in \{25, 50, 75, 100, 125\}$ °C.

Also these results indicate that the setbacks in the current Mextram model for avalanche current exists in both NPN and PNP devices.

2.4 Discussion

In previous section the measured and Mextram simulated base current (I_b) as a function of temperature for different industrial SiGe HBT technologies was presented. From the Figure 2-1, a good fit between the measured and simulated I_b as a function of temperature for the HVCOM (NPN) SiGe HBT was observed over all the bias regions with parameter values as

W_{AVL}= 576.0nm and V_{AVL}= 2.0V. Though, a good fit is observed between the measured and simulated results, but the corresponding model avalanche parameters are non-physical. For example, the parameter value of V_{AVL} should be approximately in range of the extracted base-collector built-in voltage (V_{DC} = 0.85V). Here the value of V_{AVL} is very large in comparison to V_{DC}, which indicates one of the setbacks in the current Mextram avalanche model.
On the other hand, for the HS SiGe HBT (Figure 2-2), large deviations between the measured and simulated I_b as a function of temperature were observed over the *weak avalanche* region. Similar deviations between the measured and simulated I_b as a function of temperature were observed for RFCOM (Figure 2-3) and HVCOM (PNP) (Figure 2-4) SiGe HBTs in the *weak avalanche* region.
As it can be observed from the Table 2.2, the HS SiGe HBT has the highest cut-off frequency (f_T = 137 GHz) which means higher epilayer doping concentration as compared to other measured SiGe HBTs. The higher epilayer doping concentration leads to high electric field which implies more pronounced impact ionization and avalanche effects. Therefore, the observed large deviations between measured and simulated I_b over the weak avalanche region are due to high generated local avalanche current.
For the HVCOM (NPN) SiGe HBT (Figure 2-1), no deviations between the measured and simulated base current were observed. Since the HVCOM (NPN) SiGe HBT has highest breakdown voltage, which implies lower epilayer doping concentration in comparison to the HS and RFCOM SiGe HBTs. The lower doping concentration will result in lower electric field and also the impact ionization will be less pronounced. On the other hand, the deviations between measured and simulated I_b for the HVCOM (PNP) SiGe HBT was observed (Figure 2-4) over the weak avalanche region. Here the observed deviations between the measured and simulated I_b as a function of temperature can be due to the holes which causes impact ionization in case of a PNP SiGe HBT. For the RF SiGe HBT, a smaller deviation (compared to HS SiGe HBT) between the measured and simulated base current as a function of temperature over the *weak avalanche* region was observed, which also depend on the doping concentration in the epilayer.
From these results, it is clear that the current Mextram (version 504.11.0) avalanche model is incapable of describing the avalanche current as a function of device temperature and bias for most of the modern SiGe HBT technologies. In other words the current Mextram avalanche model is technology dependent, though a global model is preferred.

2.5 Conclusion

In this chapter, the temperature dependence of avalanche current was presented by means of DC measurements and corresponding Mextram simulations for various SiGe HBT technologies. From the measured and simulated I_b over different temperatures for the different SiGe technologies, it was observed that the current Mextram avalanche model is insufficient to accurately describe the temperature dependence of the avalanche current. These observed setbacks need to be addressed. The deviations between measured and simulated I_b as a function of temperature for the HS SiGe HBT over the *weak avalanche* region was found to be the largest. For other SiGe HBT technologies like RFCOM and HVCOM (PNP) this effect was also observed but with less deviations when compared to HS SiGe HBT. Therefore, in

order to model the avalanche effect as a function of temperature properly in today's modern SiGe HBT technologies, modifications in the Mextram avalanche current model are needed. In next chapter, possible solution approaches in this direction will be discussed in detail.

CHAPTER 3

Modeling Local and Non-local Avalanche Current in Bipolar Junction Transistors

In Chapter 2 the temperature dependence of avalanche current in Mextram compact model was presented by means of DC measurements and Mextram simulations. Deviations between the measured and simulated avalanche current as function of temperature in different SiGe HBT technologies were observed. These deviations implies that there exists some setbacks in the current Mextram avalanche model that makes it unsuitable in addressing the avalanche current at different temperatures. The setbacks needs to be corrected by applying some modification in current Mextram model (version 504.11.0*). In this chapter, a summary of the avalanche process is presented first, next the electric-field based Mextram avalanche current model (local model) is discussed, and lastly the physical formulation of the non-local avalanche current model is presented.*

3.1 Avalanche Process in Bipolar Junction Transistors

In normal forward operation of a bipolar junction transistors, the base-emitter junction is forward biased and the base-collector junction is reverse biased. The large base-collector reverse bias (V_{BC}) (which implies high electric field) causes the charge carriers (electron for an NPN transistor) in the base-collector space charge region to gain enough kinetic energy so that when this carrier impacts the semiconductor atom a valence band electron gets ionized and end moving up to the conduction band. As a result of movement of an ionized electron to the conduction band a hole is generated as well. This process is known as impact ionization. Once the electron-hole pairs are generated, they are separated by the electric field, the generated holes drift towards the p-doped base and electrons towards the n-doped collector region. In the base region, a hole may take either of the two courses: it

may exit the device through the base contact without further reaction or recombine with an electron and trigger additional injection of electrons from the emitter into the base, which is basically current amplification action. The injected electrons will contribute to the increased avalanche multiplication and cause a further increase of electron injection from the emitter, forming a positive feedback loop. This process is known as avalanche multiplication and it is schematically presented in Figure 3-1. In this figure, $I_{n,in}$, is the electron current without

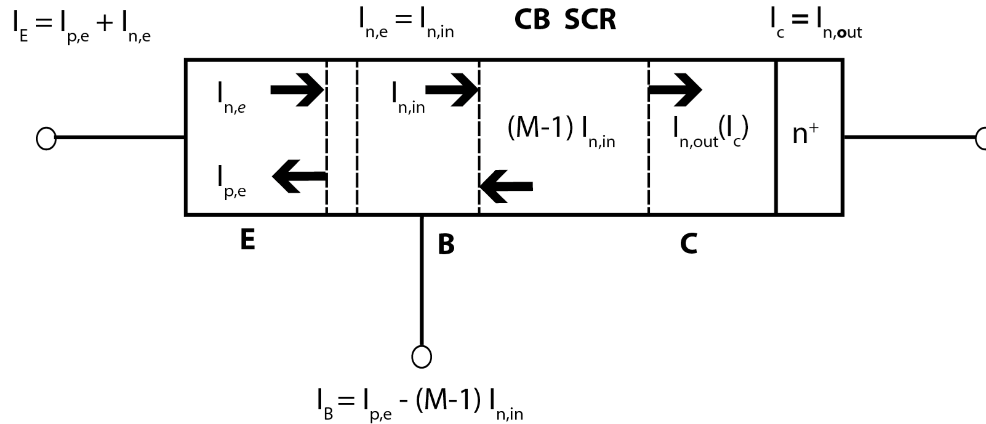

Figure 3-1: Schematic representation of the avalanche multiplication process in an NPN bipolar transistor. Due to the impact ionization in the collector-base depletion region, the hole current $(M-1)I_{n,in}$ is generated.

avalanche and $I_{n,out}$ is the electron current including avalanche. The ratio of these two current is called multiplication factor M (or (M-1)) and is defined as

$$M = \frac{I_{n,out}}{I_{n,in}}.$$

The net increase in the incident electron current due to impact ionization is equal to $I_{n,out} = MI_{n,in}$. The total base current in the base terminal I_B is reduced by $(M-1)I_{n,in}$ i.e.,

$$I_B = I_{p,e} - (M-1)I_{n,in},$$

where $I_{p,e}$ is the base current component due to the hole injection into emitter. Due to the large collector-base voltage, a reversal of I_B can be attained as a result of high generated hole current. This behavior is mostly observed in the Forward Early plots. From the Forward Early plots, the avalanche current can be defined as the difference between the base current I_B without impact ionization (very low V_{CB}) and the base current with impact ionization (high V_{CB}). This avalanche current is addressed in the Mextram model and in the next section a summary of the avalanche model in the current Mextram compact model is presented.

3.2 Modeling (Local) Avalanche Current in Mextram Model

In the current Mextram compact model (version 504.11.0), the avalanche current is modeled using a local-field characterization of the ionization rate (α). This is based on the presumption that charge carriers are instantaneously energized to a steady-state kinetic energy (threshold energy) corresponding to the high magnitude of the local electric field. In other words, it is assumed that charge carriers gains the kinetic energy to cause impact ionization upon entering the collector-base space charge region.
The full Mextram equivalent circuit for the vertical bipolar transistor is presented in Figure 3-2 [2]. In this circuit, the avalanche current is represented by a current source $\mathrm{I_{avl}}$ (marked with a dashed circle). The avalanche current is a result of the impact ionization in the epilayer

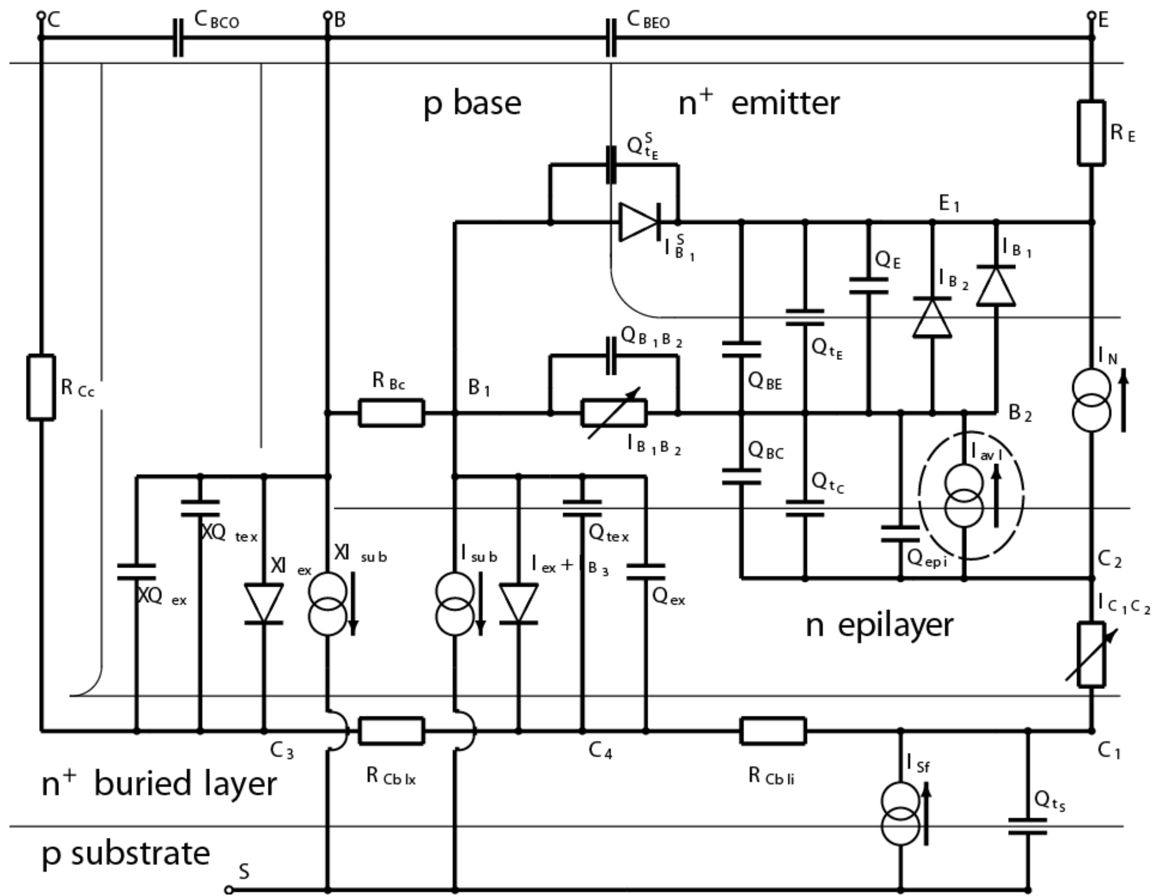

Figure 3-2: The full Mextram equivalent circuit for the vertical NPN transistor. The local avalanche current is represented by a current source $\mathrm{I_{avl}}$ (dashed circle).

due to presence of a high electric field. In Mextram model, impact ionization is defined using Chynoweth empirical law [14]

$$\alpha(E(x)) = \mathrm{A_n} \exp\left(\frac{-\mathrm{B_n}}{|E(x)|}\right), \tag{3.1}$$

where E(x) is the electric field, A_n and B_n are material constants. These two constants depends on the polarity of the transistor, hence NPN and PNP transistors will have different values. The generation of electron-hole pair is largest where the electric field is largest. Since, this is mainly in the epilayer region, hence only the impact ionization and avalanche current in the epilayer is considered. In Mextram avalanche model a simple depletion approximation is used to determine the electric field. The electric field in the epilayer is similar to electric field across a pn-junction. From the general theory of the pn-junction the integral of the electric field $(E(x))$ from the node B_2 to node C_1 (see Figure 3-2) equals to the applied collector-base voltage plus the collector-base built-in voltage V_{dc} [15]

$$-\int_{B2}^{C1} E(x)dx = -\int_{0}^{W_{epi}} E(x)dx = V_{C_1B_2} + V_{dc}. \tag{3.2}$$

Here it is assumed that the electric field in the base and in the highly doped sub-collector (buried layer) drops very fast to zero, such that the contribution to the integral only comes from the region $0 < x < W_{epi}$. Eq. (3.2) is an important limitation on the electric field , but is not sufficient to find the electric field. For this reason Gauss' law is used

$$\frac{dE}{dx} = \frac{\rho}{\varepsilon}, \tag{3.3}$$

where ρ is the total charge density and is given by

$$\rho = q(N_{epi} - n + p). \tag{3.4}$$

In the ohmic region of the epilayer, the electric field is constant and has a value

$$E = \frac{J_{epi}}{\sigma} = -\frac{I_{epi}}{\sigma\, A_{em}}, \tag{3.5}$$

where σ is the conductivity, I_{epi} is the epilayer current and A_{em} is the emitter area. In ohmic regions the electric field is low enough to prevent velocity saturation. The net charge is zero and the number of electrons equals the epilayer doping concentration N_{epi} (that is assumed to be constant). A negligible number of holes are present in the epilayer.

In the depletion region the electric field is high, hence it can be assumed that the velocity of electrons is saturated. There will be no holes in this region either. The electron density however depends on the current density. Since the electron velocity is constant, then the electron concentration in the collector epilayer $n = J_{epi}/qv_{sat}$. The total net charge density is then given by $\rho = (qN_{epi} - |J_{epi}|/v_{sat})$. For the charge density it does not matter whether the current moves forth or back. This gives the gradient of the electric field as

$$\frac{dE}{dx} = \frac{qN_{epi}}{\varepsilon}\left(1 - \frac{I_{epi}}{I_{hc}}\right), \tag{3.6}$$

where I_{hc} is the hot-carrier current and is defined as

$$I_{hc} = qN_{epi}A_{em}v_{sat}. \tag{3.7}$$

The total avalanche current is equal to the ionization coefficient multiplied by the epilayer current, integrated over all the places where ionization takes place. This hold only in the weak avalanche regime, where the generated current does not generate extra avalanche current. In this regime, the avalanche current (I_{avl}) is given by

$$I_{avl} = I_{epi} \int_0^{W_{eff}} \alpha\,[E(x)]\,dx = G_{EM}\,I_{epi}, \tag{3.8}$$

where G_{EM} is the generation factor (which needs to determined). The value W_{eff} in the integral is the effective width (the non-injected region) of the epilayer, which in normal cases is equal to W_{epi}. The width of epilayer is very important for determining the electric field. Therefore, the parameter W_{AVL} for this width is used in the avalanche model. When the epilayer current becomes negative, the epilayer will be flooded by electrons from the buried collector and the electric field is low. Hence, $I_{avl} = 0$ for the negative currents.
The most important contribution to the integral is that for the maximal electric field. For a general electric field distribution, a linearization around the maximum electric field E_{max} (see Figure 3-3) is applied:

$$|E(x)| = E_{max}\left(1 - \frac{x}{\lambda_D}\right), \tag{3.9}$$

for some given λ_D. Note, in Mextram model the absolute value of the maximum value of electric field and also its average value is taken. The electric field in Eq. (3.9) is approximated by writing

$$|E(x)| \simeq \frac{E_{max}}{\left(1 + \dfrac{x}{\lambda_D}\right)}. \tag{3.10}$$

By integration, the value of the generation coefficient is found from the electric field as

$$G_{EM} = \frac{A_n}{B_n}\lambda_D E_{max}\left\{\exp\left[-\frac{B_n}{E_{max}}\right] - \exp\left[-\frac{B_n}{E_{max}}\left(1 + \frac{W_{eff}}{\lambda_D}\right)\right]\right\}. \tag{3.11}$$

The maximum value of the electric field (E_{max}) and the extrapolation length (λ_D) still need to be determined. In the normal case (Kirk effect and current spreading in the epilayer neglected), the Mextram flag called "EXtended AVaLanche" has to be put to zero (i.e., EXAVL= 0). The extended avalanche modeling (i.e., EXAVL= 1), is not discussed in this thesis, but it can be referred from [15]. The schematic representation of the absolute value of the electric field used in derivation of the basic Mextram avalanche model in presented in Figure 3-3. The average value (absolute value) of the electric field over the depletion region is given by

$$E_{av} = \frac{V_{dc} - V_{B_2C_1}}{W_D}, \tag{3.12}$$

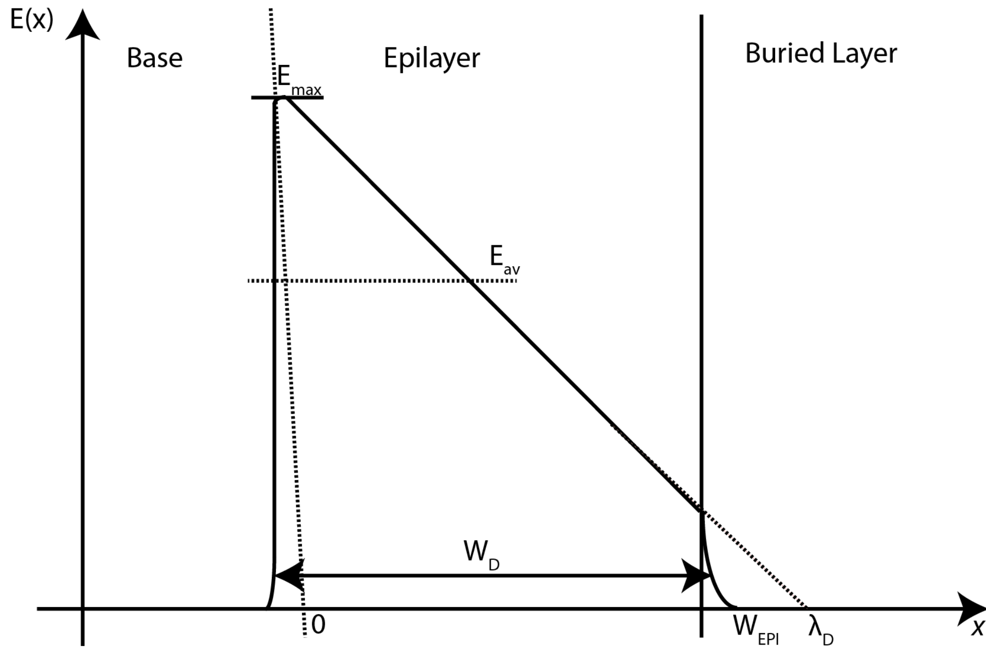

Figure 3-3: Schematic representation of the absolute value of the electric field used in the derivation of local Mextram avalanche model [2].

where W_D is the width of the depletion region. This expression suggests that the average of the electric field becomes zero when $V_{dc} = V_{B_2C_1}$. In that case the base-collector junction is already far in the forward and epilayer will be flooded with electrons and holes resulting in a low electric field. Therefore, when $V_{B_2C_1} > V_{dc}$, then $I_{avl} = 0$. Note, that the expressions below are such that the maximum of the electric field will also go to zero when its average goes to zero. The expression (Eq. (3.11)) for the generation factor is such that at that point G_{EM} will also go to zero (including all its derivatives).

At zero current, the derivative of the electric field is given by

$$\frac{dE}{dx} = \frac{q\mathrm{N_{EPI}}}{\varepsilon}\left(1 - \frac{\mathrm{I_{EPI}}}{\mathrm{I_{HC}}}\right) \Rightarrow \frac{dE}{dx} = \frac{q\mathrm{N_{EPI}}}{\varepsilon} = \frac{2\mathrm{V_{AVL}}}{\mathrm{W_{AVL}}^2}. \tag{3.13}$$

Here the second parameter of the avalanche model V_{AVL} is introduced. This parameter is therefore a measure for the derivative of the electric field, especially around the maximum electric field. For this simple and one-dimensional model it should be equal to the punch-through voltage. In practice the electric field does not really have a triangular shape especially due to non-local effects, the effective electric field is much broader around its maximum. This means that the value of V_{AVL} can become small. The direct relation with the doping level is then also lost. The electric field E_0 at the base-collector junction is calculated from Figure 3-3 as

$$\mathrm{E_0} = \mathrm{E_{av}} + \frac{1}{2}\mathrm{W_D}\ \mathrm{dEdx_0}\left(1 - \frac{\mathrm{I_{epi}}}{\mathrm{I_{hc}}}\right). \tag{3.14}$$

In normal operating regime the maximum of the electric field will be at the base-collector

junction, and therefore

$$E_{max} = E_0. \tag{3.15}$$

If, due to the reversal of the slope of the electric field (Kirk effect), the maximum of the electric field moves to the epilayer-buried layer interface, the model becomes somewhat more complex and numerically more unstable. The Mextram model also describes these effects when EXAVL = 1. In this thesis only the basic model is considered (EXAVL = 0).

Next, the extrapolation length λ_D representing the slope of electric field calculated using Eq. (3.9) can be written as

$$\left|\frac{dE}{dx}\right| = \frac{E_{max}}{\lambda_D} = dEdx_0\left(1 - \frac{I_{epi}}{I_{hc}}\right). \tag{3.16}$$

The electric field can be also written as

$$|E(x)| = E_0 - \frac{2x}{W_D}\,(E_0 - E_{av}), \tag{3.17}$$

which is given in such a way that the electric field at the middle of depletion region $x = W_D/2$ equals the average electric field $|E(W_D/2)| = E_{av}$. In the case discussed here $E_0 = E_{max}$. From the expression for the electric field, and from equation $|dE/dx| = E_{max}/\lambda_D$, the extrapolation length (λ_D) is found to be

$$\lambda_D = \frac{E_{max} W_D}{2(E_{max} - E_{av})}. \tag{3.18}$$

The thickness of the depletion layer also needs to be calculated. As mentioned before, a very simple abrupt junction depletion model is used, giving

$$W_D = \sqrt{\frac{2}{dEdx_0}}\sqrt{\frac{V_{dc} - V_{B_2C_1}}{1 - I_{epi}/I_{hc}}}. \tag{3.19}$$

This formula can lead to the depletion layers larger than the (effective) epilayer width W_{eff} (here taken to be equal to W_{AVL}). Therefore, for the thickness over which the electric field is important is empirically shaped.
The value of λ_D can not be used directly to calculate the avalanche current, because it may become very large, for instance in the iteration process of a circuit simulator, thus destroying convergency. An upper bound is considered to prevent this. There is a demand that $\lambda_D < 1$. This means that the avalanche current can never be larger than the epilayer current, which is only a trait of the weak avalanche. By substituting for E_{max} and λ_D into Eq. (3.11), the generation factor G_{EM} is obtained. Finally the substitution of G_{EM} into Eq. (3.41) yields the local avalanche current.

In this section, the local avalanche current in the Mextram model was presented. The Chynoweth's empirical rule was used to define the ionization coefficient as a function of the local-field and this was used to model the local-avalanche current (I_{avl}). By characterizing the ionization rate as a function of the carrier energy or temperature, the non-local effects can be accounted for. In the next section, non-local avalanche modeling in Mextram is discussed

in detail.

3.3 Modeling Non-local Base-Collector Avalanche Current

As mentioned earlier, the collector-epilayer doping profile influences the impact ionization and also the break down voltage, which are the important factors in high power applications. Due to presence of high electric field in base-collector space charge region of SiGe HBTs, the conventional drift-diffusion analysis which assumes locality of ionization rate is not sufficient to describe and predict the avalanche current. The electrons (for NPN transistors) travel some distance before gaining the threshold kinetic energy to cause impact ionization. The impact ionization in this case doesn't occur in corresponding to maximum electric field. The carrier energy or temperature (T_e) lags the electric field (E) and this lag is due to finite energy relaxation time of the charge carriers. Since T_e lags E, the local-electric field representation of the ionization rate (α) will overestimate the impact ionization and under estimate the collector-emitter break down voltage with an open base (BV_{CEO}).
In a non-local case α should be characterized in terms of T_e. A simplified first order energy-balance equation is used to define T_e (carrier energy) from E(x) [10].

For given electric field E(x), the carrier temperature ($T_e(x)$) can be approximated using simplified energy-balance equation which is derived by taking the second moment of Boltzmann transport equation [10, 16]

$$\frac{d\left[T_e(x)-T_o\right]}{dx}+\frac{T_e(x)-T_o}{\lambda_e}=-\frac{2q}{5k}E\left(x\right). \tag{3.20}$$

This is a first order ordinary differential equation (ODE) whose solution is given by:

$$\left[T_e\left(x\right)-T_o\right]=-\frac{2q}{5k}\int_0^x \exp\left(\frac{u-x}{\lambda_e}\right)E\left(u\right)du, \tag{3.21}$$

where T_e is the carrier temperature, T_o is the lattice temperature, and λ_e is energy relaxation length (assumed to be constant). λ_e is calculated from extensive measurement described in [10] and is equal to 650Å for pure Si bipolar junction transistors.
To determine the carrier temperature $T_e(x)$ from Eq. (3.21), the distribution E(x) should be defined. A one-dimensional model with uniform epilayer doping concentration N_{epi} is assumed in this thesis. Hence in any space-charge region (SCR) we have

$$\frac{dE}{dx}=\frac{q\left(N_{epi}-n\right)}{\varepsilon}\cong\frac{q}{\varepsilon}\left(N_{epi}-\frac{I_c}{qAv_{sat}}\right), \tag{3.22}$$

where the final approximation follows from assuming constant current in the base-collector SCR due to electrons drifting at the saturation velocity (v_{sat}). The solution of Eq. (3.22) with boundary condition $E(x=0)$, which is the electric field at the base-collector metallurgical junction is

$$E(x)=E(x=0)+\frac{qx}{\varepsilon}\left(N_{epi}-\frac{I_c}{qAv_{sat}}\right). \tag{3.23}$$

Eq. (3.23) shows, that $E(x)$ is approximately linear even when the depletion capacitance is compensated by the mobile electron charge. This linear approximation of the electric field will be used to determine the electron temperature T_e.

3.3.1 Determination of Electron Temperature $T_e(x)$

In the non-local avalanche model a linear electric field distribution in the epilayer is considered in the forward active operation mode of the transistor. The electric field distribution used in the derivation of T_e is the same as the one used to derive the Mextram local avalanche model in Section 3.2, and was presented earlier in Figure 3-3. The $E(x)$ can be approximated as linear including $E(x) = 0$ in the buried layer. Hence, E(x) in the forward active region is defined as

$$\begin{aligned} E(x) &= Ax + B, \qquad 0 < x < W_{epi} \\ &= 0, \qquad\qquad x > W_{epi} \end{aligned} \tag{3.24}$$

where A, B, and W_{epi} take on the same values as those in Figure 3-3 and they depend on the collector current and collector-base bias.
By substituting for the electric field E(x), from Eq. (3.24) into Eq. (3.21), an analytical expression for $T_e(x)$ can be calculated. Since, Eq. (3.20) is a non-homogenous ordinary differential equation, it implies that the general solution comprises of two parts, i.e., the particular solution and the homogenous solution. Therefore, the general solution $(T_e(x) - T_o)$ is given by

$$[T_e(x) - T_o] = [T_e(x) - T_o]_{particluar} + [T_e(x) - T_o]_{homogenous}. \tag{3.25}$$

Using the electric field in Eq. (3.24) over the epilayer ($0 < x < W_{epi}$) together with Eq. (3.21), the particular solution is given by:

$$\begin{aligned} -\frac{5k}{2q}[T_e(x) - T_o]_{particular} &= \int_0^x \exp\left(\frac{u-x}{\lambda_e}\right) E(u)\; du, \\ &= A\int_0^x u\; \exp\left(\frac{u-x}{\lambda_e}\right) du + B\int_0^x \exp\left(\frac{u-x}{\lambda_e}\right) du, \\ &= A\left\{\left[u\lambda_e \exp\left(\frac{u-x}{\lambda_e}\right)\right]_0^x - \left[\lambda_e^2 \exp\left(\frac{u-x}{\lambda_e}\right)\right]_0^x\right\} + \left[B\lambda_e\; \exp\left(\frac{u-x}{\lambda_e}\right)\right]_0^x, \\ &= \lambda_e\left[A\left\{x - \lambda_e + \lambda_e \exp\left(-\frac{x}{\lambda_e}\right)\right\} + B - B\; \exp\left(-\frac{x}{\lambda_e}\right)\right], \\ &= \lambda_e\left[Ax - (A\lambda_e - B) + (A\lambda_e - B)\exp\left(-\frac{x}{\lambda_e}\right)\right], \\ &= \lambda_e\left[Ax - (A\lambda_e - B)\left(1 - \exp\left(-\frac{x}{\lambda_e}\right)\right)\right]. \end{aligned} \tag{3.26}$$

The corresponding homogenous solution equal to zero i.e.,

$$[T_e(x) - T_o]_{homogenous} = 0. \tag{3.27}$$

Again using the electric field in Eq. (3.24) over the buried layer ($x > \mathrm{W_{epi}}$) together with Eq. (3.21), the corresponding particular solution is given by:

$$-\frac{5k}{2q}\left[\mathrm{T_e}\left(\mathrm{x}\right)-\mathrm{T_o}\right]_{\text{particular}} = \int_0^x \exp\left(\frac{u-x}{\lambda_\mathrm{e}}\right)\cdot 0\; du, \\ = 0. \tag{3.28}$$

By considering the homogenous part of the ODE in Eq. (3.20), the homogenous solution is

$$\left[\mathrm{T_e}\left(\mathrm{x}\right)-\mathrm{T_o}\right]_{\text{homogeneous}} = \tilde{A}\exp\left(\frac{-x}{\lambda_\mathrm{e}}\right), \tag{3.29}$$

where $\tilde{\mathrm{A}}$ is a constant of integration to be computed using the boundary condition

$$\left[\mathrm{T_e}(\mathrm{x}=\mathrm{W_{epi}})-\mathrm{T_o}\right]_{\text{homogeneous}} = -\frac{2q}{5k}\cdot\lambda_\mathrm{e}\left[A\mathrm{W_{epi}}-\left(A\lambda_\mathrm{e}-B\right)\left(1-\exp\left(-\frac{\mathrm{W_{epi}}}{\lambda_\mathrm{e}}\right)\right)\right] \tag{3.30}$$

A combination of Eq. (3.29) and Eq. (3.30), yields the homogenous solution for $x > \mathrm{W_{epi}}$ as

$$\left[\mathrm{T_e}(\mathrm{x})-\mathrm{T_o}\right]_{\text{homogeneous}} = -\frac{2q}{5k}\cdot\lambda_\mathrm{e}\mathrm{F_1}\;\exp\left(\frac{-x}{\lambda_\mathrm{e}}\right), \tag{3.31}$$

where

$$\mathrm{F_1} = \exp\left(\frac{\mathrm{W_{epi}}}{\lambda_\mathrm{e}}\right)\left[A\mathrm{W_{epi}}-\left(A\lambda_\mathrm{e}-B\right)\left(1-\exp\left(-\frac{\mathrm{W_{epi}}}{\lambda_\mathrm{e}}\right)\right)\right]. \tag{3.32}$$

Therefore a combination of Eq. (3.26), Eq. (3.27), Eq. (3.28), and Eq. (3.31), yields the general solution for the electron temperature as

$$-\frac{5k}{2q\lambda_\mathrm{e}}\left[\mathrm{T_e}\left(\mathrm{x}\right)-\mathrm{T_o}\right] = \left[Ax-\left(A\lambda_\mathrm{e}-B\right)\left(1-\exp\left(-\frac{x}{\lambda_\mathrm{e}}\right)\right)\right], \quad 0 < x < \mathrm{W_{epi}} \\ = \mathrm{F_1}\;\exp\left(\frac{-x}{\lambda_\mathrm{e}}\right), \quad x > \mathrm{W_{epi}} \tag{3.33}$$

where $\mathrm{F_1}$ is given by Eq. (3.32). A special case can be considered, whereby the electron temperature in the buried-collector ($x > \mathrm{W_{epi}}$) is taken to be zero. In that case only the solution for epi-collector is considered, and Eq. (3.33) reduces to

$$-\frac{5k}{2q\lambda_\mathrm{e}}\left[\mathrm{T_e}\left(\mathrm{x}\right)-\mathrm{T_o}\right] = \left[Ax-\left(A\lambda_\mathrm{e}-B\right)\left(1-\exp\left(-\frac{x}{\lambda_\mathrm{e}}\right)\right)\right]. \tag{3.34}$$

This electron temperature can now be used to determine the non-local avalanche current by using the Chynoweth model to determine the multiplication factor as discussed in the next section.

3.3.2 Multiplication Factor

The Chynoweth model Eq. (3.35) is use to calculate the impact-ionization rate (α) as a function of carrier temperature T_e.

$$\alpha(E(x)) = A_n \exp\left(\frac{-B_n}{|E(x)|}\right). \tag{3.35}$$

To transform Eq. (3.35), from the dependence on local-electric field ($\alpha(E(x))$) to dependence on electron temperature ($\alpha(T_e(x))$), a quasisteady-state assumption is made; i.e., $dT_e/dx = 0$. Applying the steady-state condition to Eq. (3.20) i.e.,

$$\frac{d\left[T_e(x) - T_o\right]}{dx} + \frac{\left[T_e(x) - T_0\right]}{\lambda_e} = -\frac{2q}{5k} E(x), \tag{3.36}$$

yields the solution

$$\left[T_e(x) - T_o\right] = -\frac{2q\lambda_e}{5k} E(x). \tag{3.37}$$

Rearranging the Eq. (3.37) gives,

$$|E(x)| = \frac{5k}{2q\lambda_e}\left[T_e(x) - T_o\right]. \tag{3.38}$$

By substituting Eq. (3.38) into Eq. (3.35), results into a carrier-energy or temperature dependent impact ionization rate:

$$\alpha\left[T_e(x)\right] = A_n \exp\left[-\frac{2q\lambda_e}{5k}\frac{B_n}{(T_e(x) - T_0)}\right]. \tag{3.39}$$

The electric field distribution E(x) (Eq. (3.24)), the normalized electron temperature $T_{e,n} = -(5k/2q\lambda_e)[T_e(x) - T_o]$ (Eq. (3.34)), and non-local impact-ionization rate $A = \alpha\left[T_e(x)\right]$ (Eq. (3.39)), are presented in Figure 3-4 on arbitrary vertical axis.

From Figure 3-4, it can be clearly observed that the carrier temperature lags the local-electric field. This is a result of the finite relaxation time in the non-local case.

The multiplication factor for the non-local avalanche model is defined in the same way as in the Mextram local avalanche model, but now in terms of T_e as

$$(M - 1) = \int_{EPI} \alpha\left[T_e(x)\right]\, dx, \tag{3.40}$$

with $[\alpha T_e(x)]$ defined by Eq. (3.39). This multiplication factor is used to define the compact model for the non-local avalanche current, as discussed in the next section.

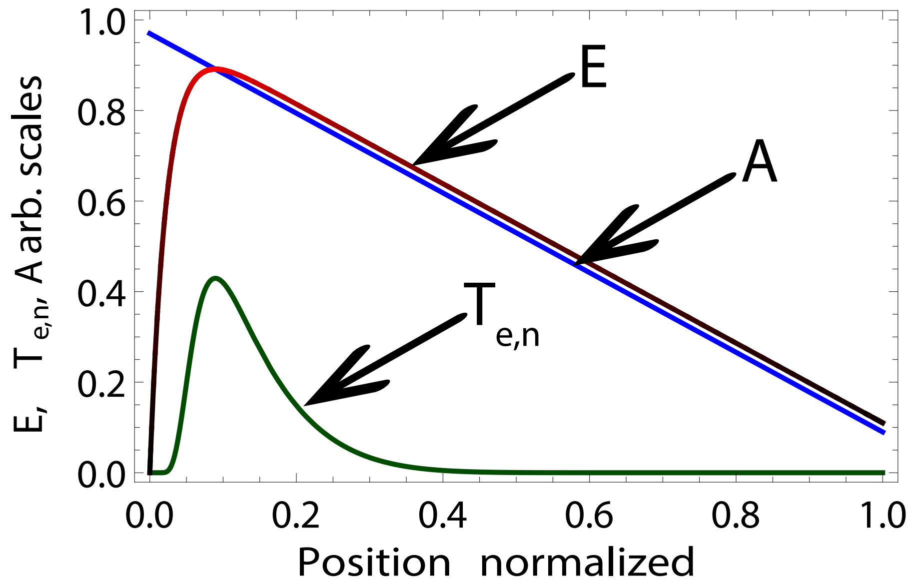

Figure 3-4: Normalized electron temperature, local-electric field, and non-local impact ionization rate in the epi-collector region under normal forward-active operational mode.

3.3.3 Compact Model for the Non-local Avalanche Current

A compact model requires an analytical expression for the integral of the ionization rate and this is the key in computing the avalanche current (both local and non-local). The non-local avalanche current I_{avl} in Mextram model is given by

$$I_{avl} = I_{epi} \int_0^{W_{eff}} \alpha \left[T_e(x)\right] dx = (M-1) I_{epi}. \tag{3.41}$$

This definition shows that the analytical express for the integral of the multiplication factor (Eq. (3.40)) need to be determined in order to have a compact formulation of the non-local avalanche current. This compact formulation of non-local avalanche current in Mextram model has been derived and implemented at Delft University of Technology, but it is beyond the scope of this thesis. Therefore, in this thesis the details about the compact model formulation of the non-local avalanche current are not discussed.
Since this thesis focuses on modeling the avalanche current as a function of temperature in Mextram model, a temperature scaling rule for the relaxation length (λ_e) and corresponding temperature coefficient used in Mextram are discussed in the next section.

3.4 Temperature Scaling of the Relaxation Length (λ_e) in Mextram Model

The non-local avalanche current model was derived taking into account that the charge carriers in base-collector space charge region travels some distance before gain enough kinetic energy to cause impact ionization. The distance traveled by the charge carriers is

the relaxation length (λ_e) as was presented earlier in Section 3.3. In the Mextram model, λ_e is represented by the model parameter L_{AVL} and the corresponding temperature coefficient by the parameter A_{LAVL}. The temperature scaling for the relaxation length in the non-local avalanche model is defined by the power law as

$$(L_{AVL})_T = L_{AVL}\left(\frac{T}{T_{ref}}\right)^{(A_{LAVL})} . \tag{3.42}$$

Here T and T_{ref} are the device and reference temperatures, respectively, and they are defined as:

$$T = TEMP + DTA + 273.15 + V_{dt},$$
$$T_{ref} = T_{ref} + 273.15,$$

where DTA is the difference between the local ambient and global ambient temperatures. V_{dt} is the increase in the device temperature ΔT due to self-heating.
L_{AVL} and A_{LAVL} are the two new non-local avalanche current model parameters introduced in Mextram. Based on [10], the default value for L_{AVL} model parameter is set to 65nm in Mextram. The "extended avalanche" flag is also extended to provide a switch to the non-local avalanche model by setting it to two (EXAVL= 2).

3.5 Summary

In this chapter, the current status of avalanche model in the Mextram was presented which is modeled locally as in [17]. The local avalanche model uses a simple depletion approximation for the local-electric field.

The physical formulation of the non-local avalanche model was presented along with the temperature scaling rule for the relaxation length. The two new non-local avalanche model parameters i.e., L_{AVL} and A_{LAVL} were introduced in the Mextram model. In Chapter 4, the verification of the non-local avalanche current model in Mextram for the different measured SiGe HBT technologies will be presented.

CHAPTER 4

Verification of the Non-local Avalanche Model in Mextram

The physical and compact model formulation of the non-local avalanche current model implemented in Mextram was presented in Chapter 3. In this chapter the parameter extraction procedure for the non-local avalanche model parameters is presented. The experimental verification of the non-local avalanche model over temperature on different measured SiGe HBT technologies is also presented.

4.1 Parameter Extraction for the Non-local Avalanche Model in Mextram

The parameter extraction procedure for the non-local avalanche model parameters is similar to that of the local avalanche current model presented in Chapter 2. In the non-local avalanche current model two new avalanche parameters L_{AVL} and A_{LAVL} i.e., relaxation length and its corresponding temperature coefficient are introduced as can be seen from Eq.(3.42). To extract the non-local avalanche model parameters (L_{AVL} and A_{LAVL}) the Mextram flag, EXtended AVaLanche is set to two (i.e., EXAVL = 2). This flag switches the Mextram from local avalanche model to non-local avalanche model. All the electrical parameters are first extracted at a reference temperature (T_{ref} = 25° C) and then temperature parameters are extracted over different temperatures as described in Section 2.2.

The avalanche current parameters, W_{AVL} and V_{AVL} are extracted at different relaxation length (L_{AVL}) in the non-local avalanche current model. First, the parameters are extracted at the reference value of L_{AVL} = 65nm, and thereafter at different values of L_{AVL}. The reference value of relaxation length is taken from the literature [10].

The avalanche current is first optimized at a reference temperature (T_{ref} = 25° C) for a fixed L_{AVL} = 65nm using the parameters W_{AVL} and V_{AVL}. The other parameters are same as those extracted in the local avalanche model by setting the flag EXAVL = 0. After extracting these two parameters, the simulated avalanche current is then optimized with respect to measured results over different temperatures by applying the temperature parameter A_{LAVL}.

Once the parameters are extracted at the L_{AVL} = 65nm, they are again extracted for different values of L_{AVL}. Here L_{AVL} values were chosen in decreasing order from L_{AVL} = 65nm and at a particular set value of L_{AVL}, the avalanche parameters W_{AVL} and V_{AVL} were extracted. A summary of extracted parameters over different values of L_{AVL} is listed in Table 4.1 for all the measured SiGe HBT technologies.

Table 4.1: Relaxation length(L_{AVL}), effective width of the epilayer for avalanche current (V_{AVL}), voltage describing the curvature of avalanche current (W_{AVL}), temperature coefficient of relaxation length (A_{LAVL}), and root-mean-square (RMS) error values extracted for the SiGe HBT technologies.

SiGe HBT Technology	L_{AVL} (nm)	W_{AVL} (nm)	V_{AVL} (V)	AL_{AVL}	RMS Error (%)
HVCOM	65.00	524.20	2.93	−0.82	1.43
(NPN)	60.00	522.60	2.77	−0.83	1.45
	52.50	520.50	2.56	−0.92	1.48
	28.39	427.70	0.75	−1.10	2.15
HS	65.00	99.00	1.15	−0.70	6.84
(NPN)	62.50	101.80	0.92	−0.70	7.06
	60.00	104.70	0.85	−0.79	6.97
	55.00	109.00	0.72	−0.92	7.69
RFCOM	65.00	231.20	2.40	−0.30	2.68
(NPN)	60.00	232.60	2.15	−0.30	2.69
	52.50	234.30	1.83	−0.35	2.71
	27.00	229.90	0.87	−0.48	2.39
HVCOM	65.00	245.30	1.43	−0.95	8.12
(PNP)	55.00	249.50	1.21	−1.10	8.16
	50.00	251.20	1.12	−1.20	8.38
	35.00	256.30	0.90	−1.20	10.39

The parameter values of temperature coefficient of relaxation length (A_{LAVL}) listed in Table 4.1, represents the optimization of the avalanche current as a function of temperature. The negative values of A_{LAVL} implies the relaxation length (L_{AVL}) decreases with increase in device temperature.
From the table it can also be observed that for all the SiGe HBT technologies the value of extracted parameter V_{AVL} decreases with decrease in L_{AVL}. It is interesting to observe, that the parameter W_{AVL} for the HS and HVCOM (PNP) SiGe HBTs increases with decrease in L_{AVL}, while for the HVCOM (NPN) and RFCOM SiGe HBTs, W_{AVL} decreases. The root-mean-square (RMS) error is also listed in Table 4.1. The RMS error determines the quality of the fitted curve and it also describes the dependency of the extracted parameters. For example in

Table 4.1, for the HVCOM (PNP) SiGe HBT for L_{AVL} = 65nm, the RMS error is 8.12%, while the RMS error at L_{AVL} = 50nm is 8.38%. From Table 4.1, it can be observed that the RMS error for extracted parameter values for all the SiGe HBT technologies do not deviate widely at different values of L_{AVL}. From the listed RMS error values it can be said that the extracted model parameters in different SiGe HBT technologies are dependent parameters.

4.2 Theoretical Calculation of the Built-in Voltage (V_{bi})

To determine the best parameter values for V_{AVL} for the different SiGe HBT technologies a comparison between the extracted V_{AVL} and theoretical built-in voltage (V_{bi}) is required, since the parameter V_{AVL} in Mextram model gives an approximation of built-in voltage. The calculation of V_{bi} will help in verifying final extracted parameter V_{AVL} values listed in Table 4.1. The built-in voltage across a junction (for Silicon) is known to be approximately given by the relation [5]

$$V_{bi} = V_{\mathrm{T}} \ \ln\left(\frac{N_A \cdot N_D}{n_i^2}\right).$$

Since the transistors used in this work are SiGe HBTs, the intrinsic carrier concentration in SiGe/Si junction will be different from that in a pure silicon junction. Hence, the above expression can be rewritten as

$$V_{bi} = V_{\mathrm{T}} \ \ln\left(\frac{N_{\mathrm{base}} \cdot N_{\mathrm{collector}}}{n_i(SiGe) \cdot n_i(Si)}\right), \tag{4.1}$$

where $V_T = kT/q$ is the thermal voltage (k is Boltzmann's constant, q is the elementary charge). N_{base} and $N_{collector}$ are the doping concentration in base and collector regions, respectively. The base in SiGe HBT is graded with germanium and the appropriate intrinsic carrier concentration is given by

$$n_i(SiGe) = n_i(Si) \ \exp\left(\frac{\Delta E_g}{2kT}\right), \tag{4.2}$$

where ΔE_g is the band-gap difference between Si and SiGe interface. The calculated ΔE_g = 0.09 eV for 20% germanium grading. Using Eq.(4.2), the calculated intrinsic carrier concentration for SiGe base is 8.5×10^{10} cm $^{-3}$.
By assuming the doping concentration in the base as $N_{base} = 1 \times 10^{18}$ cm^{-3} for all the SiGe HBTs and $N_{collector}$ as 1×10^{15} cm $^{-3}$, 5×10^{16} cm $^{-3}$, 5×10^{15} cm $^{-3}$, and 2.5×10^{15} cm $^{-3}$ for HVCOM (NPN), HS, RFCOM, and HVCOM (PNP), respectively. The corresponding calculated results for V_{bi} are presented in the Figure 4-1.

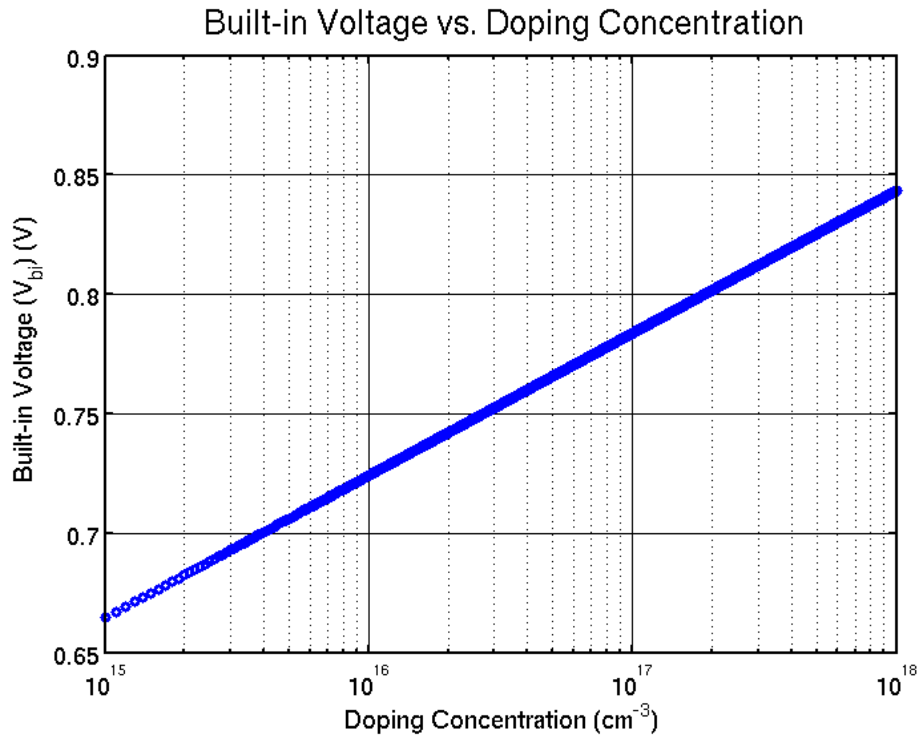

Figure 4-1: Theoretical calculated built-in voltage as a function of doping concentration in epilayer (for a fixed base doping) for the different SiGe HBTs.

4.3 Numerical Error Analysis for HS SiGe HBT

To determine the quality and accuracy of extracted parameter listed in Table 4.1, a numerical error analysis was carried for the HS SiGe HBT. In this analysis, the value of parameter V_{AVL} was fixed (V_{AVL} = 0.69V) and equal to parameter value for the extracted collector-base built-in voltage V_{DC}. The other avalanche parameters W_{AVL}, L_{AVL}, and A_{LAVL} were extracted over the temperature.
Using the same parameter values for W_{AVL}, L_{AVL} and A_{LAVL} , the final condition was disturbed (by changing the value of any of these parameters from the previous value). After changing the final condition, the avalanche current was again optimized over different temperatures and this process was repeated several times by changing the final condition.
In order to determine the influence of numerical accuracy of IC-CAP program on the parameter values, changes in the internal setting of IC-CAP were made. The Levenberg-Marquardt optimization algorithm was selected for the parameter extraction. The RMS error and max error range were reduced from 100 m to 10 m and also the parameter tolerance value was set to 1.0n in IC-CAP. The comb filter,which in IC-CAP changes the measurement data set for the simulations was employed such that half of the measured data was selected for simulations by setting comb filter value to two in IC-CAP.

The mean value (μ), standard deviation (σ), and relative error for the extracted W_{AVL}, L_{AVL}, and A_{LAVL} were calculated, and the values are listed in Table 4.2.

Table 4.2: Calculated mean (μ), standard derivation (σ), and relative error for the HS SiGe HBT for fixed V_{AVL} = 0.69V.

Parameter	Mean Value (μ)	Standard Deviation (σ)	Absolute Error (%)
W_{AVL}	104.00 nm	1.16 nm	± 2.32
L_{AVL}	62.34 nm	1.05 nm	± 2.10
A_{LAVL}	−0.96	0.032	± 0.064

The values listed in Table 4.2 represents the best extracted parameter values for the HS SiGe HBT over temperature. The absolute error (i.e., $\pm 2\sigma$) listed in Table 4.2 determines the accuracy of the extracted parameters. The absolute errors for the parameters W_{AVL}, L_{AVL}, and A_{LAVL} are small and this error range implies that the stochastic errors present in the measured data are insignificant to the final accuracy of the parameters was suggested by the experiments with comb filter in IC-CAP. The errors listed in Table 4.2 represents the accuracy of optimizations with respect to one and the same fixed set of measured data, but from different initial conditions for extracted parameters. This shows that the accuracy of the extracted model parameter values are determined by the numerical accuracy of IC-CAP, rather than by measurement errors. Also the different algorithms used for the optimization in IC-CAP will influence the accuracy of the parameters during extraction procedure.
This similar numerical error analysis can also be performed for other SiGe HBT technologies. The accuracy of the parameters extracted for the HS SiGe HBT is approximately 2% and it can be presumed that the parameter values of different SiGe HBT technologies will also have same level of accuracy.

4.4 Verification of Non-Local Avalanche Current Model

In this section the measured and Mextram simulated avalanche current as a function of temperature for different SiGe HBT technologies is presented based on the extracted parameter values. For comparing the local and non-local avalanche current models in Mextram, the results of both the models are presented in this section.

4.4.1 Verification for HVCOM (NPN) SiGe HBT

In Figure 4-2 (b), the measured (symbols) and simulated (solid lines) base current for the non-local avalanche current model as a function of temperature is presented. In order to compare results of the two avalanche models, the measured (symbols) and simulated (solid lines) base current for the local avalanche model over temperature (T_1-T_7) is also presented in Figure 4-2 (a). The Figures 4-2 (a) and (b) shows an excellent fit between the measured and simulated base current as a function of temperature for both local and non-local avalanche current models.

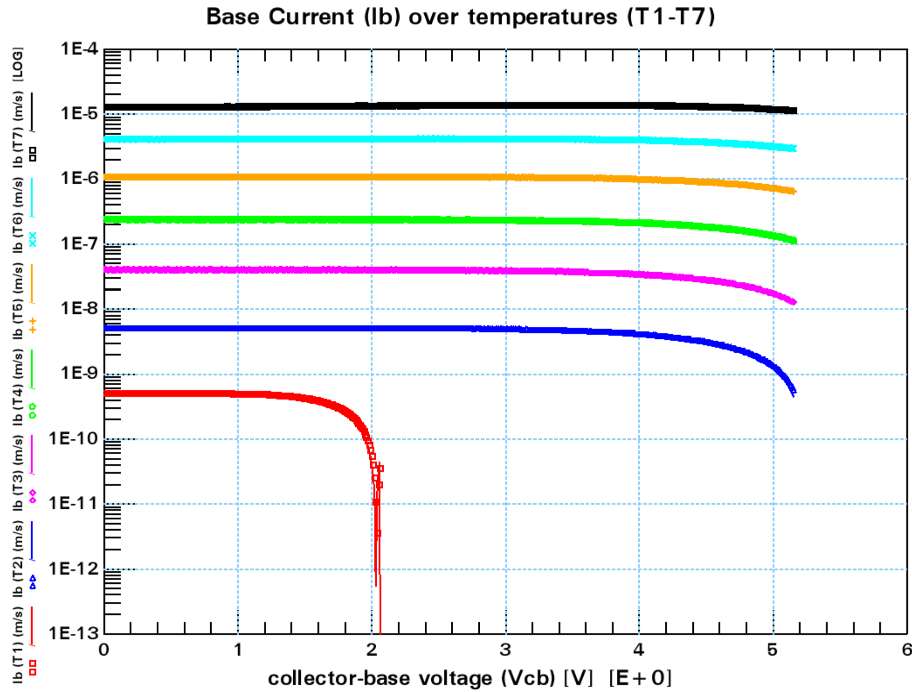

(a) Base current for the local avalanche current model.

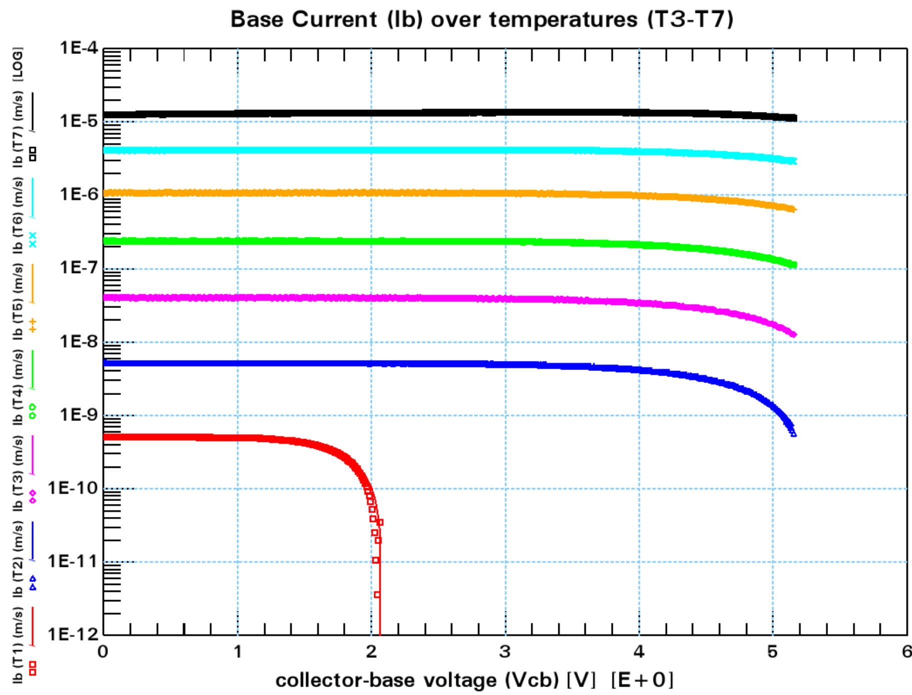

(b) Base current for the non-local avalanche current model.

Figure 4-2: Measured (symbols) and simulated (solid lines) base current as a function of collector-base voltage (V_{cb}) at seven different temperatures $T \in \{-25, 0, 25, 50, 75, 100, 125\}$ °C for HVCOM (NPN) SiGe HBT. (a) presents the local avalanche current model results with parameters $W_{AVL} = 576.0$ nm and $V_{AVL} = 2.0$ V. (b) presents the non-local avalanche current model results with $W_{AVL} = 427$ nm, $V_{AVL} = 0.75$ V, $L_{AVL} = 28.3$ nm, and $A_{LAVL} = -1.1$ as parameter values.

4.4.2 Verification Results for HS (NPN) SiGe HBT

In Figure 4-3 (b), the measured (symbols) and simulated (solid lines) base current (I_b) as a function of temperature for the non-local avalanche model is presented. The measured (symbols) and simulated (solid lines) base current (I_b) corresponding to the local avalanche current model as a function of temperature are also shown in Figure 4-3 (a).

As it can be observed from the Figure 4-3 (a), the simulated base current in the local model shows large deviations from the measured base current as a function of temperature over the *weak avalanche* region (V_{cb} >1.0V). In Figure 4-3 (b) the non-local avalanche model yields an excellent fit between the measured and simulated I_b over all temperatures and bias regions (non-local and weak avalanche regions).

This excellent fit (in Figure 4-3 (b)) of I_b over the *weak avalanche* region implies that the I_b misfit observed in Figure4-3 (a) are caused by non-local avalanche effects. Therefore, a correction of these effects is very vital for modeling avalanche effects in bipolar transistors.

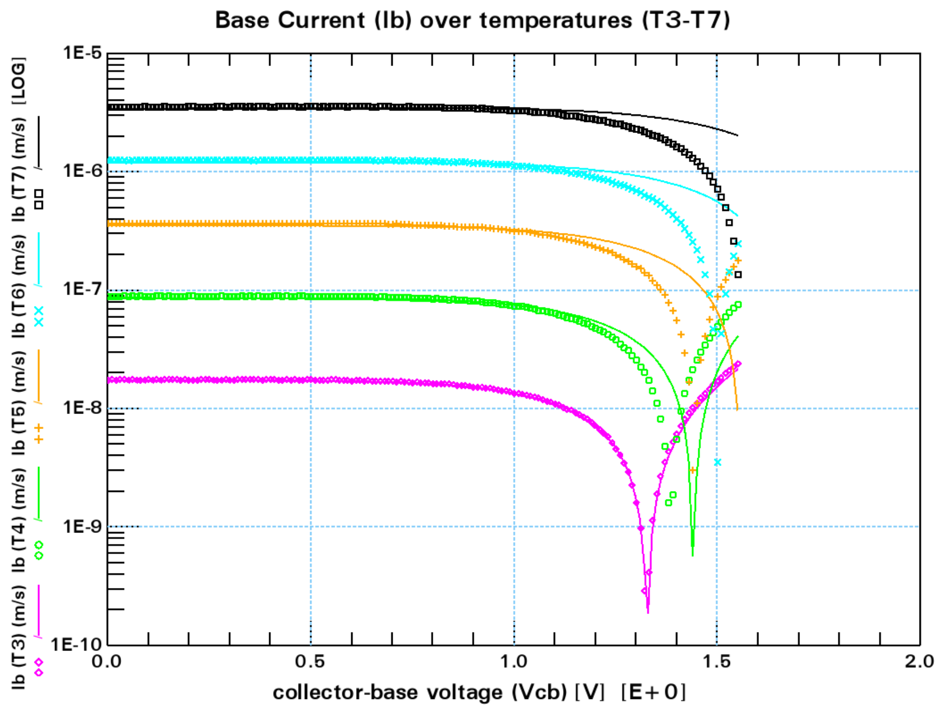

(a) Base current for the local avalanche current model

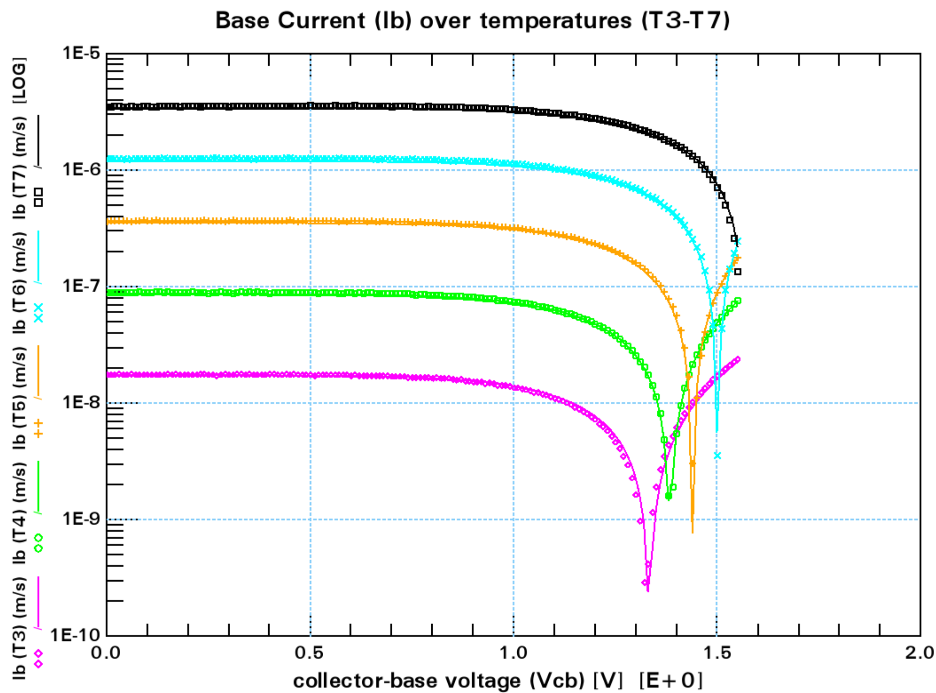

(b) Base current for the non-local avalanche current model

Figure 4-3: Measured (symbols) and simulated (solid lines) base current as a function of collector-base voltage (V_{cb}) at five different temperatures $T \in \{25, 50, 75, 100, 125\}$ °C for HS SiGe HBT. (a) presents the local avalanche current model results with parameters $W_{AVL} = 128.10$ nm and $V_{AVL} = 0.15$ V. (b) presents the non-local avalanche current model results with parameters $W_{AVL} = 104.0$ nm, $V_{AVL} = 0.69$ V, $L_{AVL} = 62.34$ nm, and $A_{LAVL} = -1.2$ as model parameter values.

4.4.3 Verification Results for RF (NPN) SiGe HBT

The measured (symbols) and simulated (solid lines) results for the base current (I_b) as a function of temperature for the non-local avalanche model are presented in Figure 4-4 (b). In Figure 4-4 (a), the measured (symbols) and simulated (solid lines) base current as a function of temperature for the local model is also presented.

From Figure 4-4 (a), deviations between the measured and I_b as a function of temperature over the *weak avalanche* region (V_{cb} >2.0V) are observed. The non-local avalanche model yields excellent fit between measured and simulated I_b as a function of temperature over all bias regions.

As in the HS SiGe HBT, the good fit in Figure 4-3(b) implies that the deviations between the measured and the simulated I_b over the *weak avalanche* region are caused by the neglected non-local effects. A correction for these effects yields good results as can be seen in the Figure 4-4 (b).

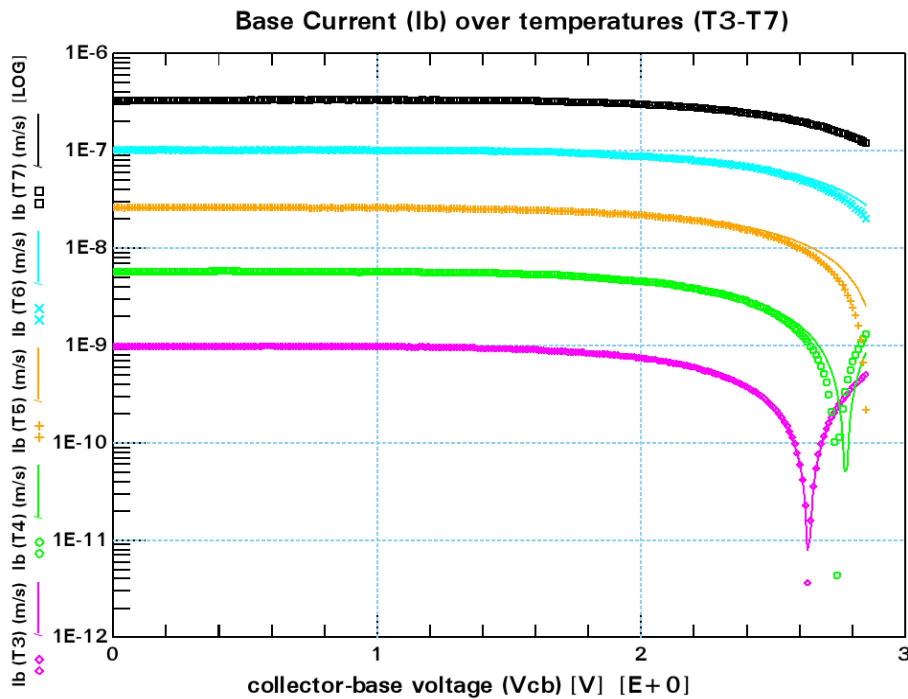

(a) Base current for the local avalanche current model.

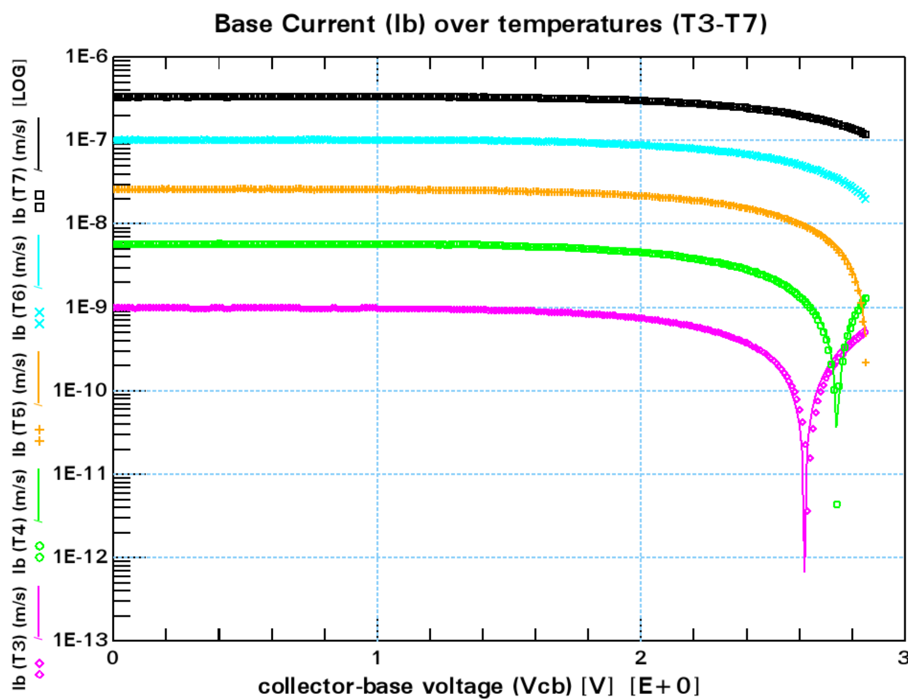

(b) Base current for the non-local avalanche current model.

Figure 4-4: Measured (symbols) and simulated (solid lines) base current as a function of collector-base voltage (V_{cb}) at five different temperatures $T \in \{25, 50, 75, 100, 125\}$°C for RF SiGe HBT. (a) presents the local avalanche model results with parameters $W_{AVL} = 261.0$ nm and $V_{AVL} = 0.80$ V. (b) presents the non-local avalanche model results with $W_{AVL} = 229.9$ nm, $V_{AVL} = 0.87$ V, $L_{AVL} = 27.0$ nm, and $A_{LAVL} = -0.48$ as parameter values.

4.4.4 Verification Results for HVCOM (PNP) SiGe HBT

For the HVCOM (PNP) SiGe HBT, the measured (symbols) and simulated (solid lines) base current (I_b) as a function of temperature for the non-local avalanche model is presented in the Figure 4-5 (b). The measured (symbols) and simulated (solid lines) avalanche current for the local model over temperature is also presented in the Figure 4-5 (a).

In Figure 4-5 (a), simulated results corresponding to the local avalanche current model shows a misfit between the measured and simulated I_b as a function of temperature over the *weak avalanche* region (V_{cb} >3.5V). On the other hand, in Figure 4-5 (b), it can be observed that by correction for the non-local effects, an excellent fit between measured and I_b (as a function of temperature) is achieved over all bias regions (non-avalanche and weak avalanche region).

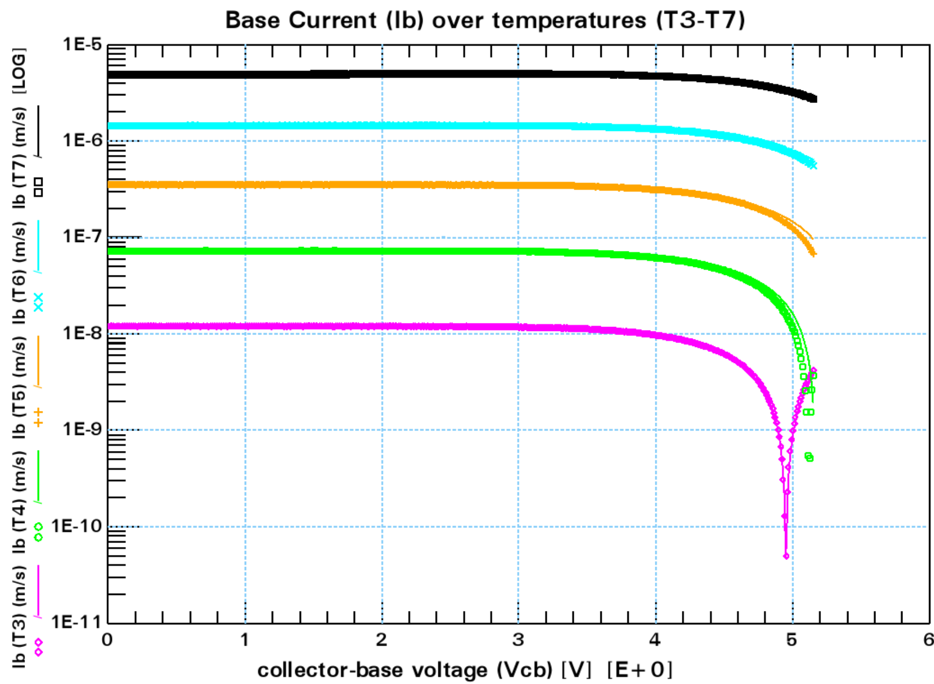

(a) Base current for the local avalanche current model.

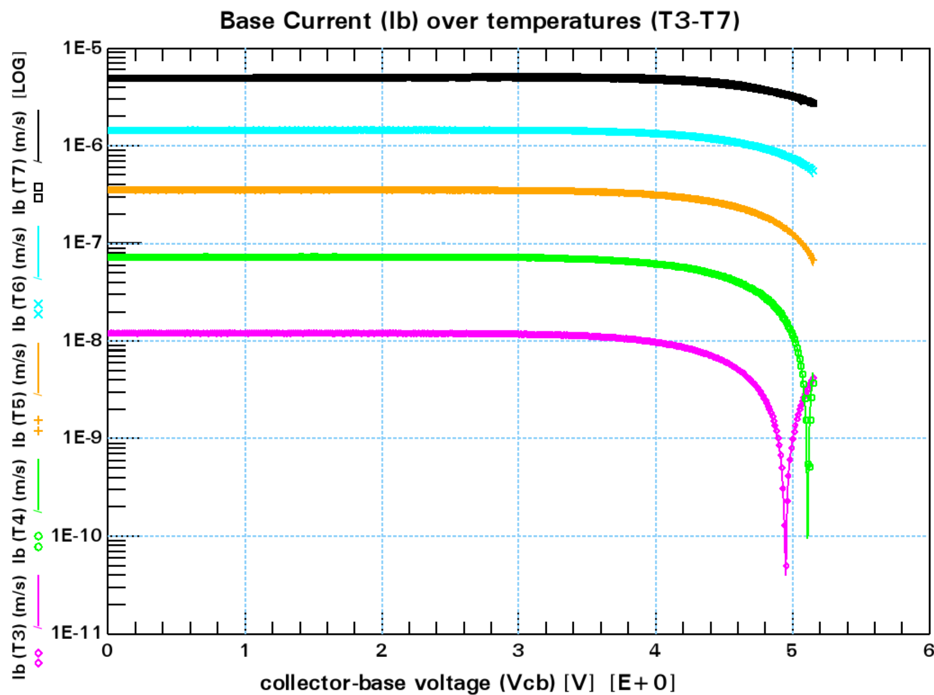

(b) Base current for the non-local avalanche current model.

Figure 4-5: Measured (symbols) and simulated (solid lines) base current as a function of collector-base voltage (V_{cb}) at five different temperatures $T \in \{25, 50, 75, 100, 125\}$ °C for HVCOM (PNP) transistor. (a) presents the local avalanche model results with parameters W_{AVL} = 272.1 nm and V_{AVL} = 0.89 V. (b) presents the non-local avalanche model results with W_{AVL} = 256.3 nm, V_{AVL} = 0.9 V, L_{AVL} = 35 nm, and $A_{LAVL} = -1.2$ as parameter values.

4.5 Discussion

In the previous section results for the measured and simulated base current (I_b) for the non-local avalanche model as a function of temperature were compared with those from the local avalanche current model. It was observed that I_b as a function of temperature for the non-local avalanche model yields excellent fits for all different SiGe HBT technologies over the *weak avalanche* bias region. This was not the case for the local avalanche current model results. This results implies that the misfits observed from the local avalanche current model results over the *weak avalanche* region are caused by the non-local effects. These effects are addressed in the non-local avalanche current model and hence a global fit is achieved for all SiGe HBT technologies.

Also in this section, the final extracted parameter values for the non-local avalanche model are presented and discussed. In Table 4.3, these values for all the measured transistor technologies are presented.

Table 4.3: Parameter values for different transistor technologies extracted for the non-local avalanche model.

SiGe HBT Technology	W_{AVL} (nm)	V_{AVL} (V)	V_{DC} (V)	L_{AVL} (nm)	A_{LAVL}
HVCOM (NPN)	427.7	0.75	0.85	28.3	−1.10
HS (NPN)	104.0	0.68	0.69	62.3	−0.96
RFCOM (NPN)	229.9	0.87	0.88	27.0	−0.48
HVCOM (PNP)	256.3	0.90	0.90	35.0	−1.20

The parameters listed in Table 4.3 are selected from the extracted parameter values presented in Table 4.1. As it can be observed from Table 4.1, the values listed in Table 4.3 do not represents the best-fitted curves as the RMS error values are not minimum (except RFCOM transistor). The parameter values in this table are selected depending on the corresponding parameter value of V_{AVL}. From Table 4.3, it is clear that the parameter value V_{AVL} for the different SiGe HBT technologies are close to the extracted base-collector built-in voltage (V_{DC}). The parameter V_{AVL} extracted at the reference value of relaxation length i.e., at L_{AVL} = 65nm has a higher value compared to the V_{DC}. The parameter values of V_{AVL} of L_{AVL} = 65nm are non-physical. As described before, the parameter V_{AVL} in Mextram should be in the range of V_{DC}.

The value of the relaxation length parameter L_{AVL} listed in this table have different values from 65nm as published in [10]. The published value of the relaxation length was for pure silicon transistors and L_{AVL} appears to be a material dependent property. In this thesis the transistors used during measurements were SiGe HBTs and it can be possible to have different values of relaxation length for different SiGe HBTs with different germanium grading in the base. Therefore, the different SiGe HBT technologies have different values of relaxation length in comparison to the one reported in [10].

4.6 Conclusion

In this chapter, experimental verification of non-local avalanche current model on different industrial SiGe HBTs was presented. The non-local avalanche model addresses the temperature dependence of the avalanche current. This model demonstrated a good agreement between measured and simulated avalanche current as a function of temperature (as was presented in Section 4.4). The new non-local avalanche model takes into account the temperature dependence of relaxation length for the charge carriers. It has been experimentally verified that the value of relaxation length varies for different SiGe HBT technologies. The relaxation length was found to be shorter compared to the reference value of 65 nm as reported in literature. Adding the germanium in the base of transistor changes the mechanical stress and due to mechanical stress the lattice will be deformed which in turn reduces the relaxation length. For reliable compact modeling results, the avalanche current in Mextram should be modeled taking in account non-local effects. The extracted parameter values for both NPN and PNP SiGe HBTs were also discussed. Also, the accuracy of the extracted parameters was calculated and discussed.

CHAPTER 5

Conclusion and Recommendations

This chapter presents concluding remarks for the verification of non-local avalanche model in Mextram which was carried out during the course of this thesis. Additionally, areas requiring further exploration are identified and highlighted in the recommendation section.

5.1 Conclusions

This thesis started with DC measurements on several advanced industrial SiGe HBTs with the focus on studying and analyzing the temperature dependence of avalanche current in Mextram compact model. From the measurement and Mextram simulation results, it was shown that the existing Mextram avalanche current model is incapable of addressing the temperature dependence of avalanche current. This setback was more pronounced for HS SiGe HBT with highly doped and short epilayer. The same issue was also observed for other SiGe HBT technologies like RFCOM and HVCOM (PNP). Hence, for accurately modeling the avalanche current as a function of device temperature in Mextram model, modifications were made in existing Mextram avalanche model.

A hypothesis was made to include non-local avalanche effects in the avalanche current. In Chapter 3, a simplified energy-balance equation was used to define the impact ionization rate (α) in terms of the carrier energy or electron temperature (T_e) rather than the local-field (E). An electric field distribution corresponding to the normal forward operational was used to determine (α [(T_e)]). The same local-field distribution is used to define the current local avalanche Mextram model. By assuming a quasi-steady state condition, the multiplication factor (M-1) was defined in terms of the electron temperature dependent impact-ionization rate (α [(T_e)]), over the collector epilayer. A multiplication of the multiplication factor with epilayer current (I_{epi}) in Mextram yielded the required non-local impact ionization

(avalanche) current. The compact formulation of the impact ioninzation integral over the epilayer was derived and simulated in the in-house Mextram model at Delft University of Technology.

Two new non-local avalanche Mextram model parameters L_{AVL} and A_{LAVL} were introduced together along with a EXAVL flag extended to two. This flag switches the avalanche current model in Mextram from local model to non-local model. An experimental verification of the new non-local avalanche model in Mextram was carried out in Chapter 4, using the measurements carried on the measured SiGe HBT technologies. From the verification of the non-local model, a good agreement was achieved between measured and simulated results for the base current in all the operational regions. Therefore, by correcting non-local effects, the new non-local avalanche model implemented in Mextram can describe accurately the avalanche current as a function of device temperature.

5.2 Main Findings

The main finding after the verification of the non-local avalanche model for different SiGe HBT technologies are summarized below.

- The non-local avalanche model which was added to the TU Delft in-house experimental version of Mextram yielded excellent agreement between the measured and simulated avalanche current as a function of temperature for all measured SiGe HBT technologies.
- The extracted model parameter values for the non-local avalanche model are physical plausible in contrast to local avalanche model parameters.
- As part of the verification effort, the experimental value of the relaxation length for SiGe HBTs appears to be shorter compared to the relaxation length for pure silicon transistors as published in literature.
- As the out come of the experimental verification performed in this thesis, it was observed that the relaxation length is inversely proportional to the temperature coefficient of the relaxation length for the measured SiGe HBT technologies (expect for RFCOM SiGe HBT).

5.3 Recommendations

The following topics would be interesting to study in a future reference.

- The parameter V_{DC} in Mextram model in some parts is used as the built-in voltage parameter for the collector-base junction and in some other parts it is a measure for the doping concentration in the epilayer. Hence, the future release of Mextram model can have two separate parameters i.e., one for the built-in voltage and another for the description of the epilayer doping concentration.
- The non-local avalanche current model address only the weak avalanche current i.e., it is assumed that during the process of impact ionization no extra charge carriers are

generated. The non-local model can also be extended to include the strong avalanche current.

- The numerical error analysis can also be performed for the other SiGe HBTs as mentioned in Section 4.2, to determine the accuracy of extracted parameters for those SiGe HBTs.

- Due to limitation of the measuring equipments, the DC measurements for certain SiGe HBTs were unreliable especially at lower temperatures (i.e., $T_1 = -25$ °C and $T_2 = 0$ °C). It will be interesting to investigate the behavior of the relaxation length and the corresponding temperature coefficient at lower temperatures.

- It would be very interesting to investigative the possible effects of the non-local avalanche effects on the RF behavior of the transistor.

- In the development of the non-local avalanche current model, a local electric field distribution corresponding to the normal forward active operation mode was assumed. It would be interesting to extend this model to electric field distributions corresponding to other operational modes such as total depletion of the epilayer, non-ohmic quasi saturation, and hard saturation. In addition, collector current spreading effect can also be addressed as in the case of the local avalanche model.

APPENDIX A

Measurement and Simulation Results for HVCOM SiGe HBTs

In this appendix, the measurement and Mextram simulations results for the HVCOM (NPN) and HVCOM (PNP) SiGe HBTs are presented.

A.1 Measurement and Simulation Result for HVCOM (NPN) SiGe HBT

A.1.1 Depletion Capacitance Measurements and Mextram Simulations Results

Base-Emitter Depletion Capacitance (C_{be})

The base-emitter depletion capacitance measurements were carried out as a function of base-emitter voltage (V_{be}) and temperature (T_1- T_7). The measured (symbols) and simulated (solid lines) results for C_{be} as a function of temperature and V_{be} are presented in Figure A-1. From Figure A-1, good fit between the measured and simulated results for base-emitter depletion capacitances can be observed over the temperature.

Base-Collector Depletion Capacitance (C_{bc})

The base-collector capacitance is measured as a function of base-collector voltage (V_{bc}) and temperatures (T_1-T_7). The measured (symbols) and simulated (solid lines) results of C_{bc} as a function of temperature and V_{bc} are presented in Figure A-2.
A good agreement can be observed from Figure A-2, between measured and simulated results for base-collector depletion capacitances as a function of device temperature.

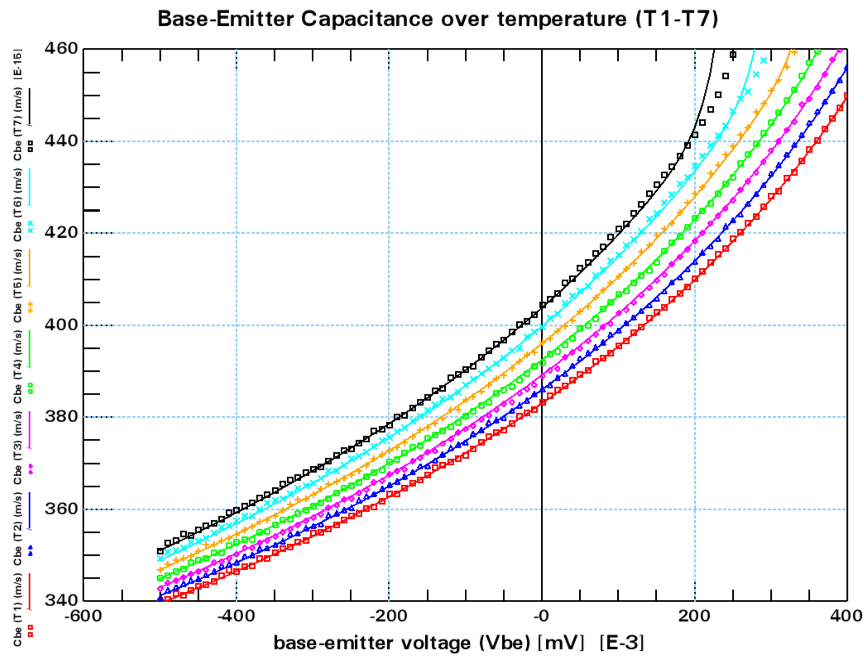

Figure A-1: Measured (symbols) and simulated (solid lines) base-emitter depletion capacitance (C_{be}) as a function of base-emitter voltage (V_{be}) and temperature $T \in \{-25, 0, 25, 50, 75, 100, 125\}$ °C.

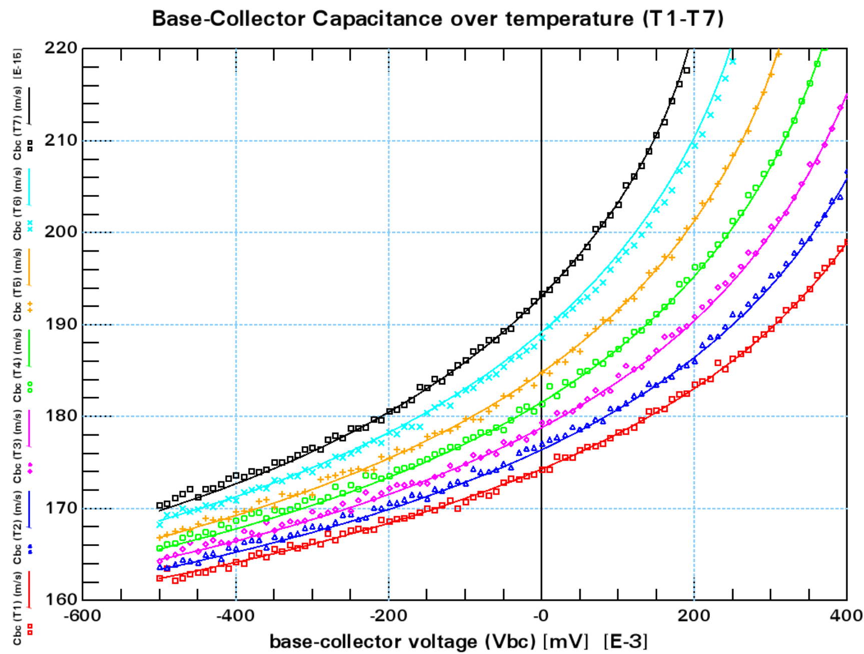

Figure A-2: Measured (symbols) and simulated (solid lines) base-collector depletion capacitance (C_{bc}) as a function of base-collector voltage (V_{bc}) and temperature $T \in \{-25, 0, 25, 50, 75, 100, 125\}$ °C.

A.1.2 Forward Gummel Measurement and Mextram Simulation

The Forward Gummel measurements were carried out as a function of base-emitter voltage (V_{be}) and temperature. The measured (symbols) and simulated (solid lines) results for the base current (I_b) and collector current (I_c) as a function of temperature are presented in Figures A-3 and A-4, respectively. The different operation regions of the transistor i.e., non-ideal region, ideal region, and, high-current region can be observed from these figures. An excellent fit between measured and simulated results for I_c and I_b in the non-ideal and ideal-regions is achieved over temperature (T_1-T_7). There is a misfit between measured and simulation results in the high-current region for temperatures T_5, T_6, and T_7. It can be neglected since the model parameters that were relevant for describing the avalanche current are extracted over the ideal and non-ideal regions.

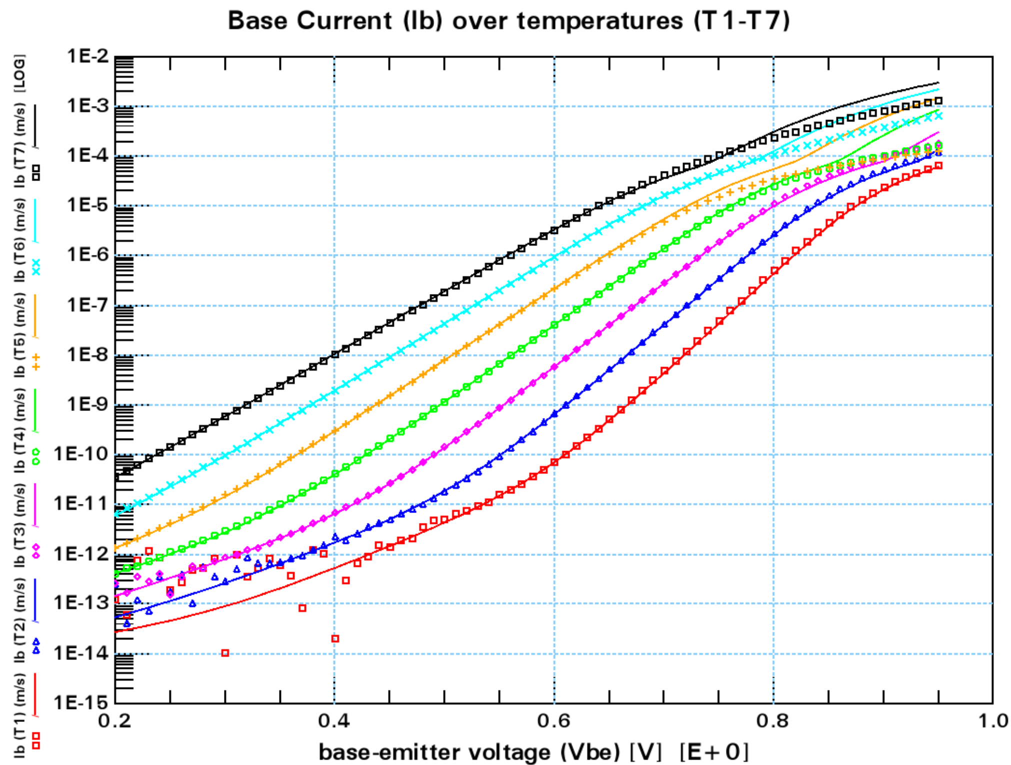

Figure A-3: Measured (symbols) and simulated (solid lines) base current (I_b) as a function of base-emitter voltage (V_{be}) and temperature $T \in \{-25, 0, 25, 50, 75, 100, 125\}$ °C.

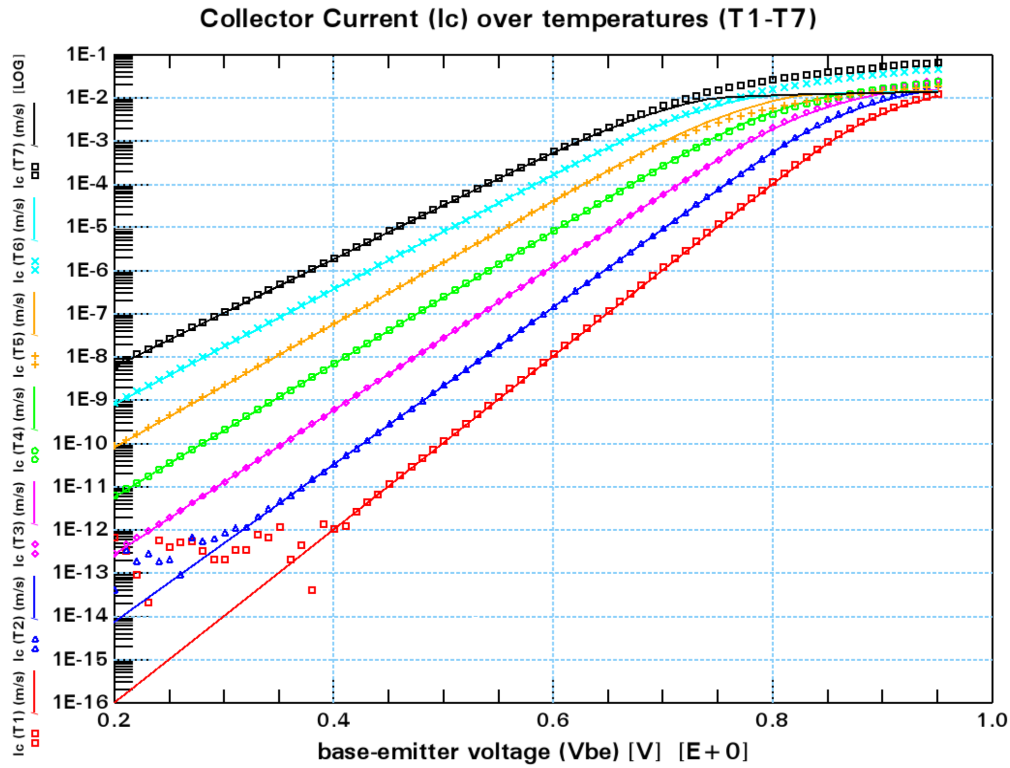

Figure A-4: Measured (symbols) and simulated (solid lines) collector current (I_c) as a function of base-emitter voltage (V_{be}) and temperature $T \in \{-25, 0, 25, 50, 75, 100, 125\}$ °C.

A.1.3 Reverse Gummel Measurement and Mextram Simulation

The Reverse Gummel measurements were carried out as a function of V_{bc} and temperature. The measured (symbols) and simulated (solid lines) results for the I_b and I_e as a function of temperature for HVCOM (NPN) SiGe HBT are presented in Figures A-5 and A-6, respectively.

The different transistor operation regions can be identified as non-ideal region, ideal region, and high-current region. From the Figures A-5 and A-6, a good agreement between measured and simulated results for the I_b and I_e in the non-ideal and ideal regions can be observed for all device temperatures. A mismatch between measured and simulated results for I_b and I_e in high-current region at temperatures T_5, T_6, and T_7 is observed. Similar to Forward Gummel measurements, the misfits in the high-current region can be neglected as the relevant Reverse Gummel model parameters are extracted in the non-ideal and ideal regions.

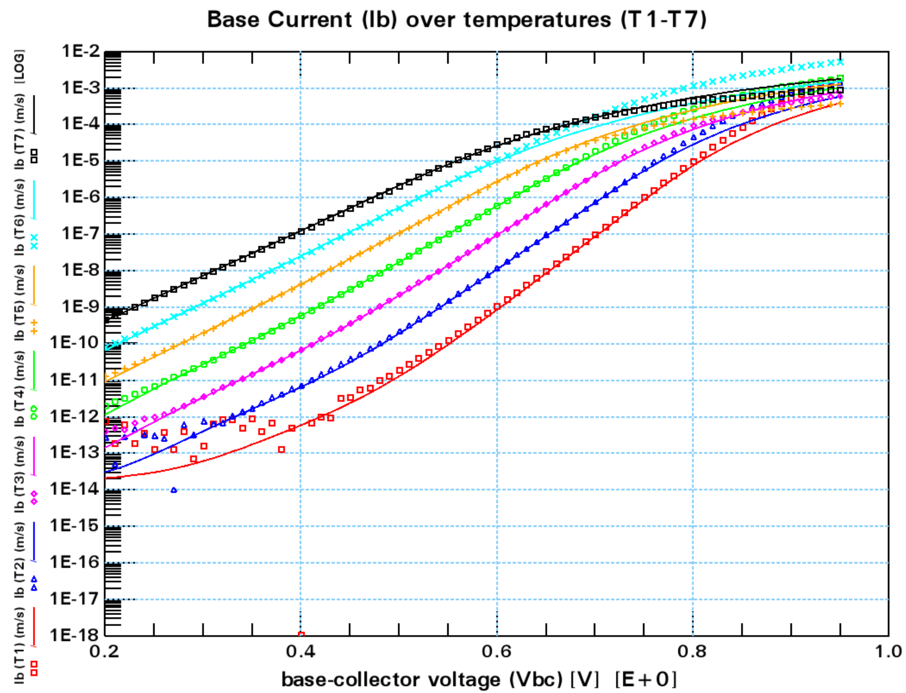

Figure A-5: Measured (symbols) and simulated (solid lines) base current (I_b) as a function of base-collector voltage (V_{bc}) and temperature $T \in \{-25, 0, 25, 50, 75, 100, 125\}$ °C.

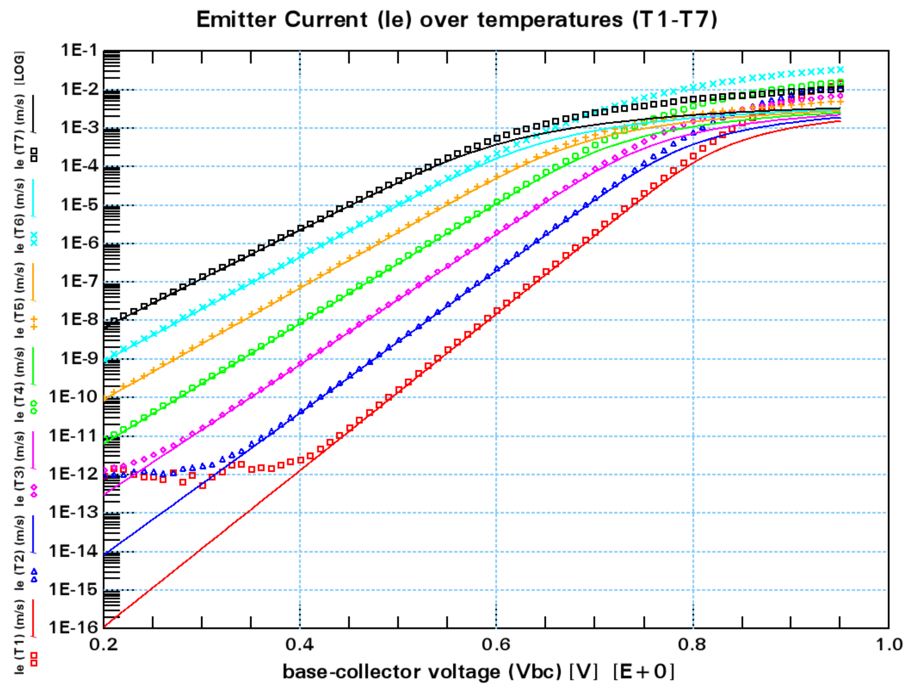

Figure A-6: Measured (symbols) and simulated (solid lines) emitter current (I_e) as a function of base-collector voltage (V_{bc}) and temperature $T \in \{-25, 0, 25, 50, 75, 100, 125\}$ °C.

A.1.4 Forward Early Measurement and Mextram Simulation

The measured (symbols) and simulated (solid lines) results for collector current (I_c) as a function of collector-base voltage (V_{cb}) and temperature are presented in Figure A-7.
It is clear from the Figure A-7, that there is a good agreement between the measured and simulated results for I_c as a function of V_{cb} and temperature.

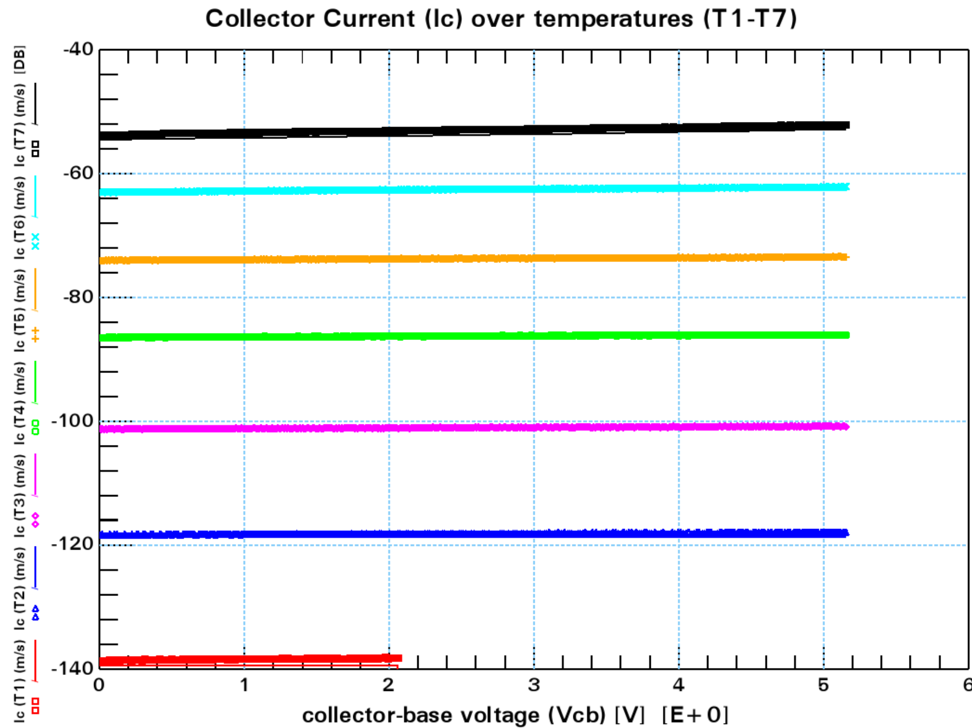

Figure A-7: Measured (symbols) and simulated (solid lines) collector current (I_c) as a function of collector-base voltage (V_{cb}) and temperature $T \in \{-25, 0, 25, 50, 75, 100, 125\}$ °C.

A.1.5 Output Characteristics Measurements and Mextram Simulations

These measurements were performed at constant base-currents $I_b = 5\ \mu A$, $10\ \mu A$, and $15\ \mu A$ and various device temperatures. The collector current (I_c) (Figure A-8) and the base-emitter voltage (V_{be}) (Figure A-9), were measured as functions of collector-emitter voltage (V_{ce}). The various regions i.e., quasi-saturation, ideal, and avalanche regions can be identified from this figure. In order, to avoid over-crowding in plot, only the measured (symbols) and simulated (solid lines) results corresponding to $T_3 = 25$ °C are represented.

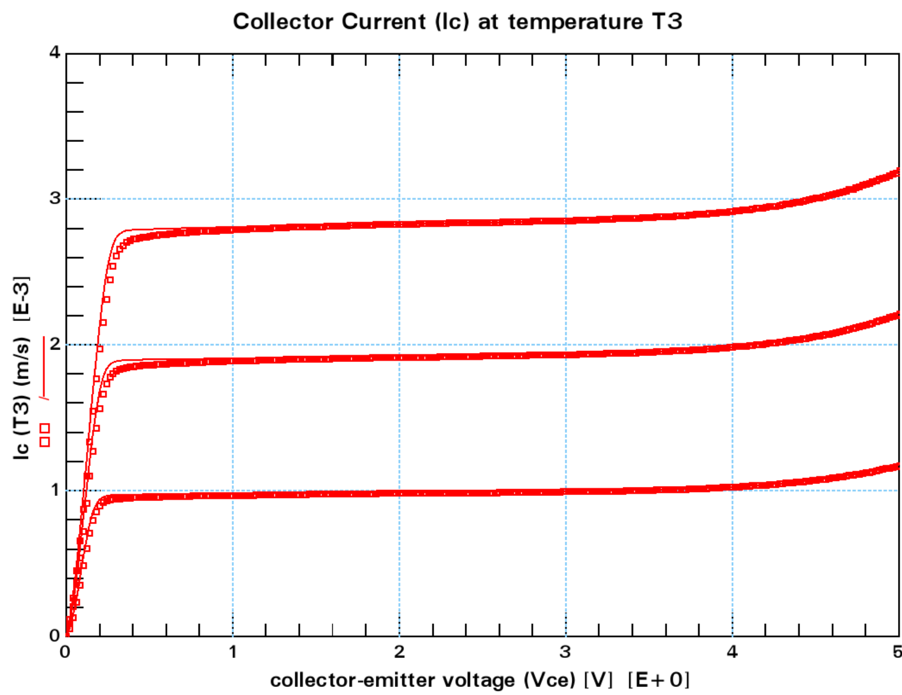

Figure A-8: Measured (symbols) and simulated (solid lines) collector current (I_c) as a function of collector-emitter voltage (V_{ce}) at temperature (T_3)°C.

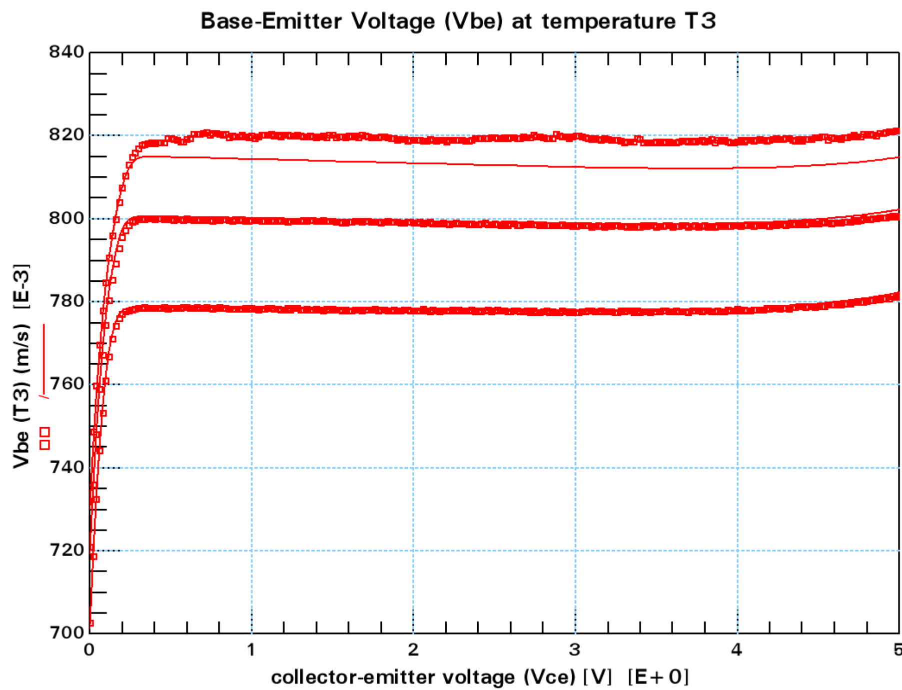

Figure A-9: Measured (symbols) and simulated (solid lines) base-emitter voltage (V_{be}) as a function of collector-emitter voltage (V_{ce}) at temperature (T_3) °C.

A.2 Measurement and Simulation Result for HVCOM (PNP) SiGe HBT

The measurement and Mextram simulation results for the HVCOM (PNP) SiGe HBT are presented in this section. The measurements and simulations in the PNP SiGe HBT is similar to those of the corresponding NPN transistor, only the biasing is reversed and the holes are mostly responsible for main current. All the conclusions from the measured and simulated results can be interpreted exactly the same way as for the NPN transistor.

A.2.1 Depletion Capacitance Measurement and Mextram Simulation Results

Base-Emitter Depletion Capacitance (C_{be})

The measured (symbols) and simulated (solid lines) base-emitter capacitance (C_{be}) are presented in Figure A-10. From the Figure A-10, a good fit between measured and simulated results for base-emitter capacitance over all the temperatures is observed.

Base-Collector Depletion Capacitance (C_{bc})

The measured (symbols) and simulated (solid lines) base-collector depletion capacitance as a function of temperature is presented in Figure A-11.
In the Figure A-11, a good agreement between measured and simulated results for the base-collector depletion capacitance is obtained over all the temperatures.

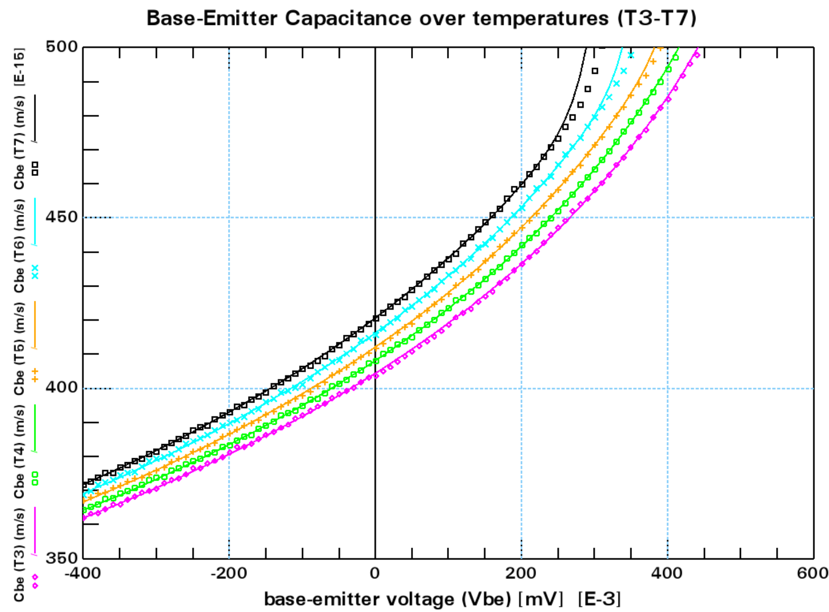

Figure A-10: Measured (symbols) and simulated (solid lines) base-emitter depletion capacitance (C_{be}) as a function of base-emitter voltage (V_{be}) and temperature $T \in \{25, 50, 75, 100, 125\}$ °C.

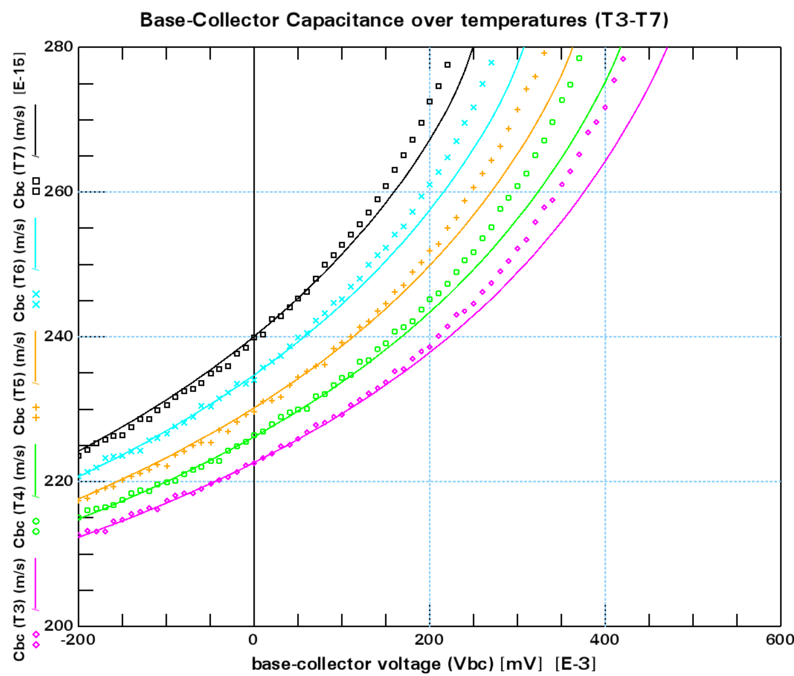

Figure A-11: Measured (symbols) and simulated (solid lines) base-collector depletion capacitance (C_{bc}) as a function of base-collector voltage (V_{bc}) and temperature $T \in \{25, 50, 75, 100, 125\}$ °C.

A.2.2 Forward Gummel Measurement and Mextram Simulation Results

The measured (symbols) and simulated (solid lines) results for the base current (I_b) and collector current (I_c) are presented in Figures A-12 and A-13, respectively. As it can be observed from the Figures that the I_b and I_c increases with temperature. The different operation regions non-ideal, ideal, and high-current regions can be observed. An good fit between measured and simulated results for I_b and I_c are achieved over the temperatures (T_1-T_7).

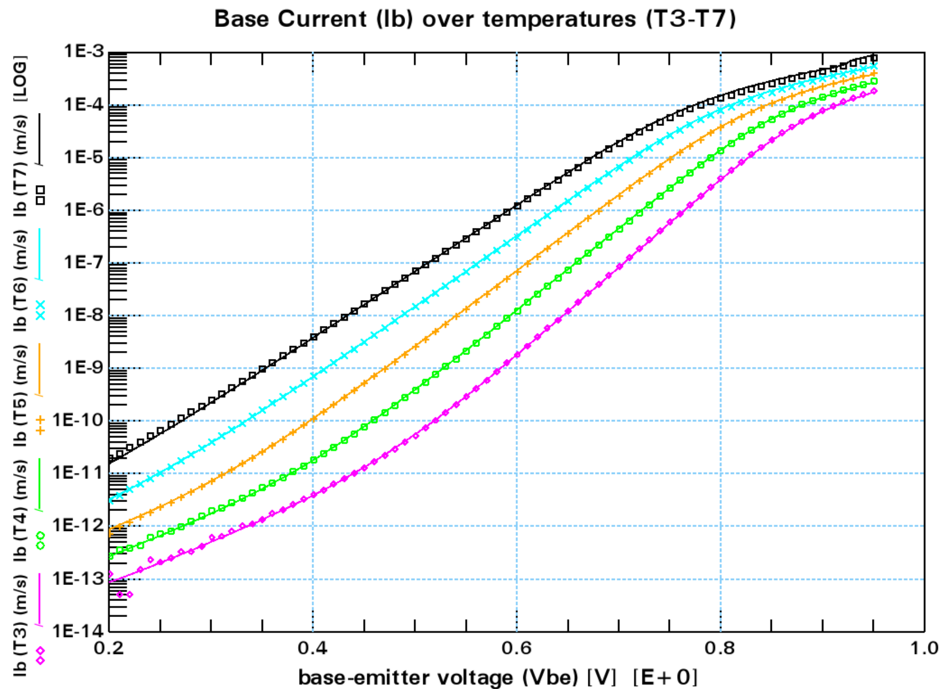

Figure A-12: Measured (symbols) and simulated (solid lines) base current (I_b) as a function of base-emitter voltage (V_{be}) and temperature $T \in \{25, 50, 75, 100, 125\}$ °C.

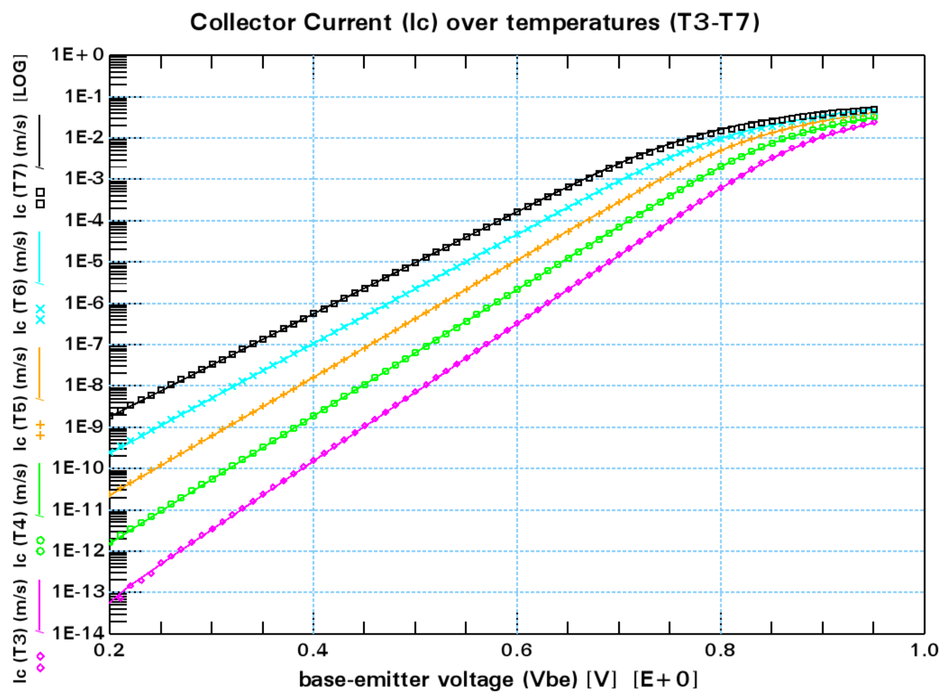

Figure A-13: Measured (symbols) and simulated (solid lines) collector current (I_c) as a function of base-emitter voltage (V_{be}) and temperature $T \in \{25, 50, 75, 100, 125\}$ °C.

A.2.3 Reverse Gummel Measurement and Mextram Simulation Results

The measured (symbols) and simulated (solid lines) results for the I_b and I_e are presented in Figures A-14 and A-15, respectively. From the Figures A-14 and A-15 a good agreement between measured and simulated results for I_b and I_e over all the temperatures can be observed.

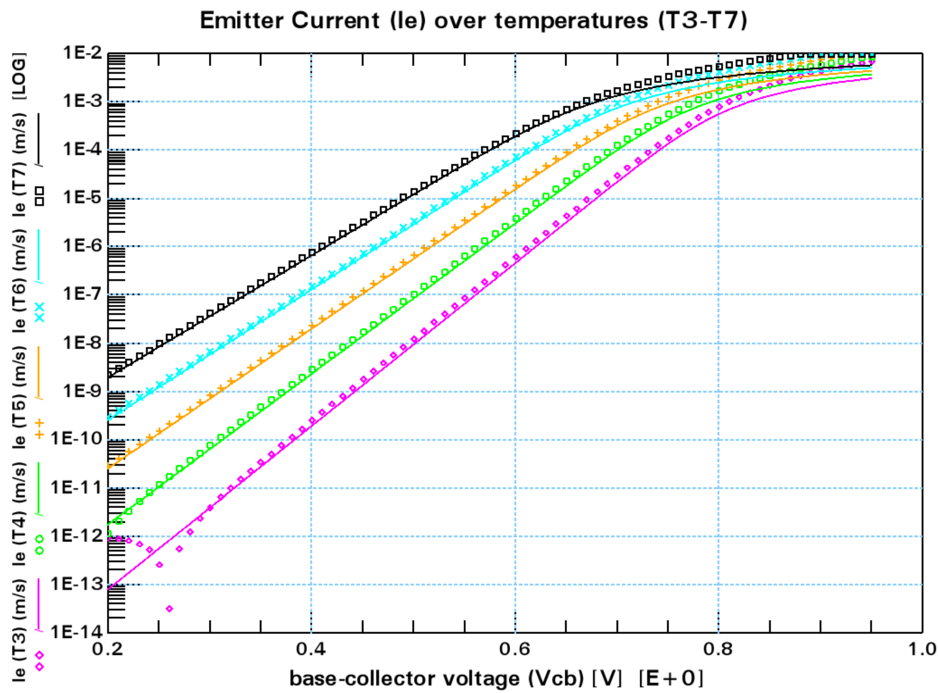

Figure A-14: Measured (symbols) and simulated (solid lines) emitter current (I_e) as a function of base-collector voltage (V_{bc}) and temperature $T \in \{25, 50, 75, 100, 125\}$ °C.

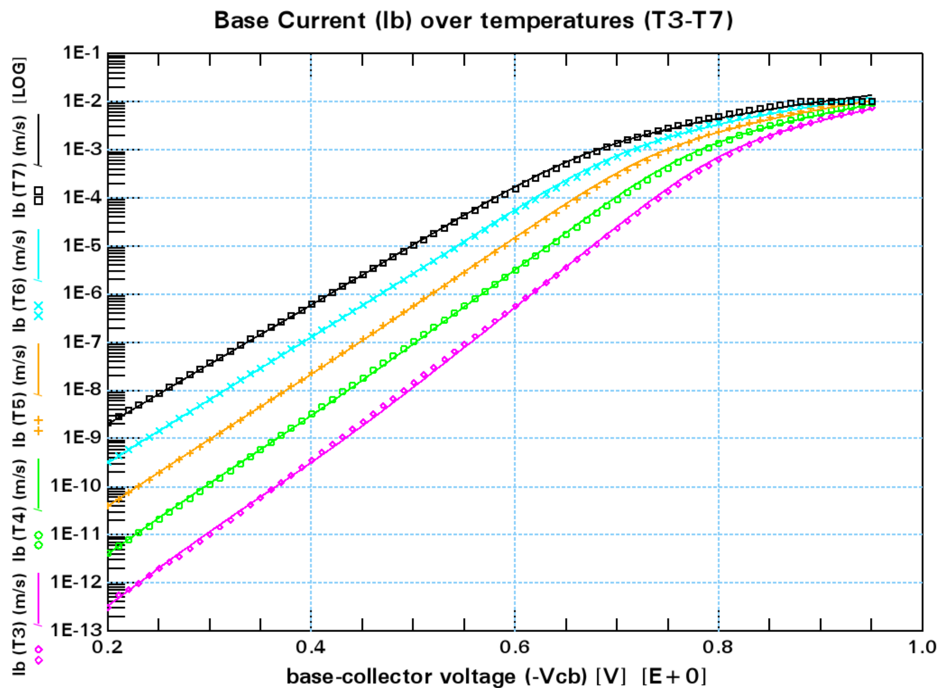

Figure A-15: Measured (symbols) and simulated (solid lines) base current (I_b) as a function of base-collector voltage (V_{bc}) and temperature $T \in \{25, 50, 75, 100, 125\}$ °C.

A.2.4 Forward Early Measurement and Mextram Simulations Results

The measured (symbols) and simulated (solid lines) results for collector current (I_c) as a function of collector-base voltage(V_{cb}) and temperature are presented in the Figure A-16.

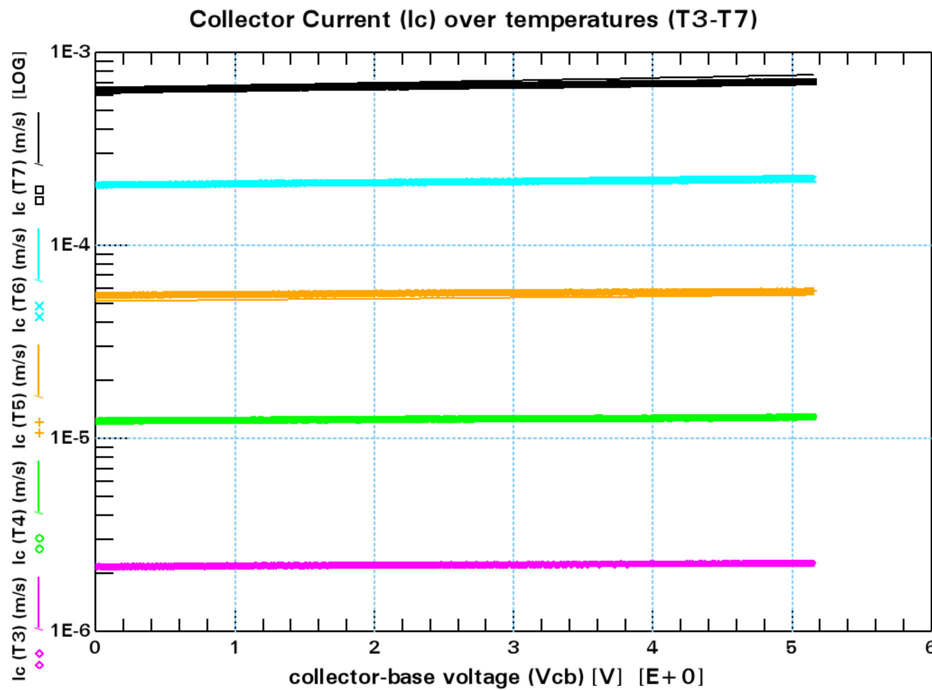

Figure A-16: Measured (symbols) and simulated (solid lines) collector current (I_c) as a function of collector-base voltage (V_{cb}) and temperature T ∈ {25, 50, 75, 100, 125} °C.

A.2.5 Output Characteristics Measurement and Mextram Simulation Results

These measurements were performed at constant base-currents I_b = 5 μA, 10 μA, and 15 μA and various temperatures. In order, to avoid over-crowding in plot, only the measured (symbols) and simulated (solid lines) results corresponding to T=25 °C are represented in Figures A-17 and A-18.

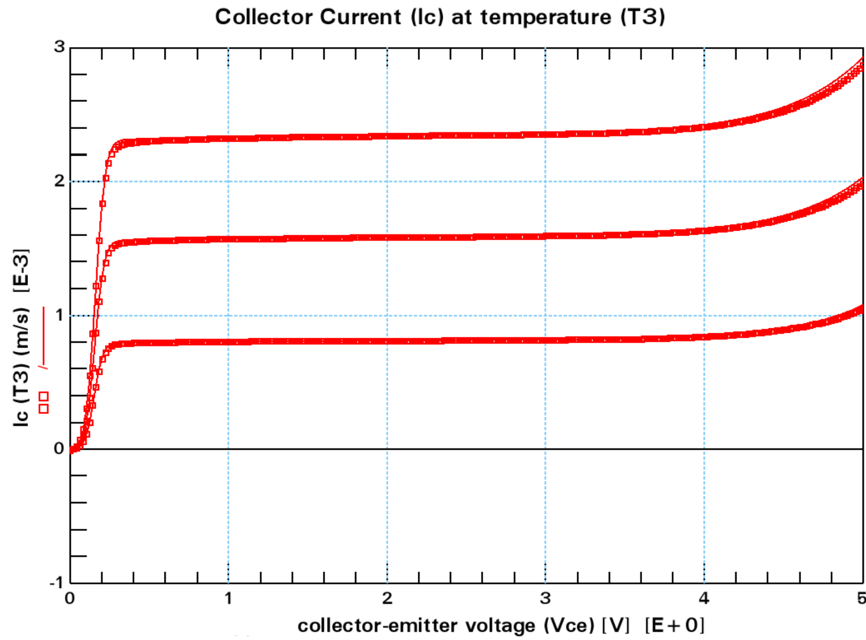

Figure A-17: Measured (symbols) and simulated (solid lines) collector current (I_c) as a function of collector-emitter voltage (V_{ce}) at temperature T_3=25°C.

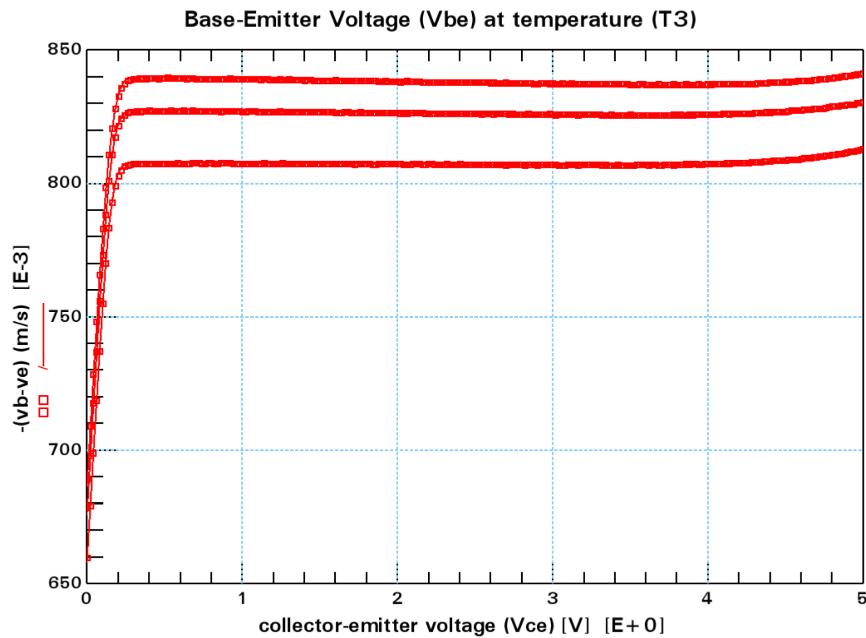

Figure A-18: Measured (symbols) and simulated (solid lines) base-emitter voltage (V_{be}) as a function of collector-emitter voltage (V_{ce}) at temperature T_3=25°C.

Bibliography

[1] John D. Cressler, Guofu Niu, *Silicon-Germanium Heterojunction Bipolar Transistors*. Artech House, 2003.

[2] Mextram homepage. [Online]. Available: http://mextram.ewi.tudelft.nl/

[3] E. Johnson, "Physical limitations on frequency and power parameters of transistors," in *IRE International Convention Record*, vol. 13, 1965, pp. 27–34.

[4] Peter Ashburn, *SiGe Heterojunction Bipolar Transistors*. John Wiley & Sons Ltd, 2003.

[5] K. S. M.Sze, *Physics of semiconductor devices*. John Wiley & Sons, 2007.

[6] Ebers, J. J. and Moll, J. L., "Large-Signal Behavior of Junction Transistors," *Proceedings of the IRE*, vol. 42, no. 12, pp. 1761–1772, 1954.

[7] M. Schröter, "Staying current with HICUM," *Circuits and Devices Magazine, IEEE*, vol. 18, no. 3, pp. 16–25, 2002.

[8] C. McAndrew, J. Seitchik, D. F. Bowers, M. Dunn, M. Foisy, I. Getreu, M. McSwain, S. Moinian, J. Parker, D. Roulston, M. Schroter, P. Van Wijnen, and L. Wagner, "VBIC95, the vertical bipolar inter-company model," *Solid-State Circuits, IEEE Journal of*, vol. 31, no. 10, pp. 1476–1483, 1996.

[9] Compact model coalition. [Online]. Available: http://www.si2.org/cmc_index.php

[10] J. Slotboom, G. Streutker, M. van Dort, P. Woerlee, A. Pruijmboom, and D. Gravesteijn, "Non-local impact ionization in silicon devices," in *Electron Devices Meeting, 1991. IEDM '91. Technical Digest., International*, 1991, pp. 127–130.

[11] V. Milovanovic, "Advanced Breakdown Modeling for Solid-State Circuit Design," Ph.D. dissertation, TU Delft, the Netherlands, 2010.

[12] P. Deixler, A. Rodriguez, W. De Boer, H. Sun, R. Colclaser, D. Bower, N. Bell, A. Yao, R. Brock, Y. Bouttement, G. A. M. Hurkx, L. Tiemeijer, J. Paasschens, H. Huizing, D. Hartskeerl, P. Agrarwal, P. H. C. Magnee, E. Aksen, and J. Slotboom, "QUBiC4X: An f_T/f_{max} = 130/140 GHz SiGe: C-BiCMOS manufacturing technology with elite passives for emerging microwave applications," in *Bipolar/BiCMOS Circuits and Technology, 2004. Proceedings of the 2004 Meeting*, 2004, pp. 233–236.

[13] IC-CAP 2011, Agilent Technologies, 2011 .

[14] A. G. Chynoweth, "Ionization rates for electrons and holes in silicon," *Phys. Rev.*, vol. 109, pp. 1537–1540, Mar 1958.

[15] J. C. J. Paasschens, W. J. Kloosterma, and R. van der Toorn, "Model Derivation of Mextram 504, The physics behind the model," Philips Research Eindhoven, Technical note TN-2004/01010, 2005.

[16] E. Crabbe, J. M. C. Stork, G. Baccarani, M. Fischetti, and S. Laux, "The impact of non-equilibrium transport on breakdown and transit time in bipolar transistors," in *Electron Devices Meeting, 1990. IEDM '90. Technical Digest., International*, 1990, pp. 463–466.

[17] W. Kloosterman, J. Paasschens, and R. Havens, "A comprehensive bipolar avalanche multiplication compact model for circuit simulation," in *Bipolar/BiCMOS Circuits and Technology Meeting, 2000. Proceedings of the 2000*, 2000, pp. 172–175.

Acknowledgments

I intentionally kept the acknowledgments part for the end. Not only did I want for it to be the last pages of my thesis, but I also wanted for it to be the last words I would ever write for my masters. And I wanted these words to be spent on thanking all the people without whom writing this thesis would not have ever been possible.

First and foremost, I would like to express my sincere gratitude to my supervisor Dr. ir. Ramses van der Toorn for his immense help, guidance and supervision throughout this thesis. I would like to extend my thanks to my daily supervisor ir. Robert Setekera for his help, guidance and motivation during this thesis. I appreciate his immense patience and also for encouraging me to finish this thesis on time.

I would also like to express my sincere gratitude to Prof. Ronald Dekker and Dr. ir. Jaap Hoekstra for serving on my thesis defense committee. It is my privilege to have Prof. Jan Slotboom as well, in my thesis defense committee.

I was fortunate to have some good colleagues with whom I shared the M.Sc. student room. It was great to have Catello, Giovanni, Hong Wah, Sourish, and Iuri in the same room. I had great time with each and every one of these people and I thank them for this wonderful time.

I would now like to thank all my friends and roommates in Delft with whom I have shared all my sweet memories and bitter experiences. I would like to thank Vishwas, Shekhar, and Ravi, I had wonderful and memorable time with them. I was fortunate to have such friends who always supported me during my tough times in Delft. Ravi has been like an elder brother to me, whom I can call any time of the day and talk for hours. I also want to thank Abhijit, Akshay, Anirban, Ankit, Gaurav, Maruti, Nandish, Nishant, Shreyas and Sneha for the good times that I have spent with them during my stay in Delft. It gives me great pleasure to also thank Sumeet Kumar for all his thoughtful advices and suggestions during my masters.

My special thanks goes to my dear Greek friends, Eirini and Nicko. I had a memorable time with them in Delft and I would like to thank them for everything that they have done for me. I wish both of them good luck for the future.

I would like to extend my special thanks to Luisa. She has been my good friend and running coach in Delft. I had her good company during my long runs and thanks a lot for always

keeping me motivated for running (especially during sub-zero temperatures). She has always been very supportive during the rough phases of my thesis.

I would like express my whole hearted gratitude to a special person in the Netherlands, John Stals. I can't dream of crossing the finish line without him. He was always there when I needed him the most, whether it was a financial problem or personal issues. I am short of words for his care, love, support and motivation throughout my masters.

Lastly, but most importantly, I want to thank my family in India. Whatever I am and whatever I have achieved so far in my life, is because of my family. My father has always encouraged me to listen to my heart and chase my dreams. It is the sacrifices and hardships of my mother that has always given me an opportunity for a better education and to be a better human being. I appreciate my younger sister's constant care and love during all my difficult times. Without the sacrifices of my parents and sister, this journey wouldn't have been completed and so I would like to dedicate this thesis to them.

Dhariyash Rathod
Delft, The Netherlands
December 12, 2013